

## RESEARCH ARTICLE

10.1002/2016JD026184

## Key Points:

- A new directional model is developed for tropospheric horizontal gradients in GPS analysis
- The new gradient model significantly improves GPS height estimates during extreme and unusual weather situations
- The use of the new gradient model can change the estimates of tropospheric zenith delays by up to 15 mm

## Supporting Information:

- Supporting Information S1

## Correspondence to:

S. Masoumi,  
salim.masoumi@anu.edu.au

## Citation:

Masoumi, S., S. McClusky, A. Koulali, and P. Tregoning (2017), A directional model of tropospheric horizontal gradients in Global Positioning System and its application for particular weather scenarios, *J. Geophys. Res. Atmos.*, 122, 4401–4425, doi:10.1002/2016JD026184.



Received 3 NOV 2016

Accepted 26 MAR 2017

Accepted article online 3 APR 2017

Published online 18 APR 2017

## A directional model of tropospheric horizontal gradients in Global Positioning System and its application for particular weather scenarios

Salim Masoumi<sup>1</sup> , Simon McClusky<sup>1</sup>, Achraf Koulali<sup>1</sup>, and Paul Tregoning<sup>1</sup> 

<sup>1</sup>Research School of Earth Sciences, Australian National University, Canberra, ACT, Australia

**Abstract** Improper modeling of horizontal tropospheric gradients in GPS analysis induces errors in estimated parameters, with the largest impact on heights and tropospheric zenith delays. The conventional two-axis tilted plane model of horizontal gradients fails to provide an accurate representation of tropospheric gradients under weather conditions with asymmetric horizontal changes of refractivity. A new parametrization of tropospheric gradients whereby an arbitrary number of gradients are estimated as discrete directional wedges is shown via simulations to significantly improve the accuracy of recovered tropospheric zenith delays in asymmetric gradient scenarios. In a case study of an extreme rain event that occurred in September 2002 in southern France, the new directional parametrization is able to isolate the strong gradients in particular azimuths around the GPS stations consistent with the “V” shape spatial pattern of the observed precipitation. In another study of a network of GPS stations in the Sierra Nevada region where highly asymmetric tropospheric gradients are known to exist, the new directional model significantly improves the repeatabilities of the stations in asymmetric gradient situations while causing slightly degraded repeatabilities for the stations in normal symmetric gradient conditions. The average improvement over the entire network is ~31%, while the improvement for one of the worst affected sites P631 is ~49% (from 8.5 mm to 4.3 mm) in terms of weighted root-mean-square (WRMS) error and ~82% (from –1.1 to –0.2) in terms of skewness. At the same station, the use of the directional model changes the estimates of zenith wet delay by 15 mm (~25%).

### 1. Introduction

Since the advent of Global Positioning System (GPS), the delay in GPS L-band frequency signals caused by the presence of atmospheric water vapor molecules has been used for monitoring temporal and spatial changes of the troposphere using permanent ground-based GPS stations. The information retrieved from GPS observations is generally in the form of zenith total delay (ZTD) or equivalent precipitable water vapor (PWV) above the GPS site [Bevis *et al.*, 1992]. Some research has been dedicated to investigating the relationship between water vapor accumulation and precipitation systems [e.g., Champollion *et al.*, 2004; Van Baelen *et al.*, 2011]. In a recent study by Labbouz *et al.* [2015], it was shown that the PWV reached its maximum on average 20 min prior to precipitation maximum for 76% of the cases for a midlatitude site in France, using 5 years of GPS and rain gauge measurements. Although such studies are still in early stages, and despite the unknown complications of weather systems, there still seems to be demand for further work on horizontal movements of the moisture in the atmosphere and the link with the formation of extreme precipitation events.

GPS-derived zenith delays have also been used as input data for operational assimilation systems [e.g., Bennitt and Jupp, 2012]. However, we are currently limited to the use of zenith delays for assimilation purposes, since the line-of-sight delays suffer greatly from unmodeled site-specific effects, mapping function errors, and deficiencies in modeling the tropospheric horizontal gradients. Since GPS observations are made at different elevation and azimuth angles around the site, mapping functions are used to map the delay from the observing angle to the zenith angle above the site [e.g., Niell, 1996; Böhm *et al.*, 2006a, 2006b]. Such mapping functions generally assume that the troposphere is symmetric around the GPS site and thus only depend on the elevation angle of observations and not on the azimuthal direction of the signal. However, horizontal heterogeneities in the tropospheric refractivity field are known to exist [e.g., Gardner, 1976; Davis *et al.*, 1993; Gegout *et al.*, 2011]; therefore, most geodetic analysts estimate additional linear horizontal gradient parameters in the form of north-south and east-west components [Chen and Herring, 1997]. Such a gradient

model assumes that the troposphere is a plane with linear horizontal changes in zenith delay. While this is a reasonable approximation for most situations, there are cases when a plane does not well represent the atmospheric refractivity field. Such cases occur, for instance, when there is a strong moisture content in a specific direction at a site.

There have been attempts to better represent the asymmetry of the troposphere by using azimuth-dependent mapping functions rather than estimating linear gradients. *Böhm et al.* [2005] performed a line-of-sight ray tracing every 30° in azimuth through interpolated slant refractivity profiles from the European Centre for Medium-Range Weather Forecasts (ECMWF) Numerical Weather Model (NWM) to derive asymmetric mapping functions called Vienna Mapping Functions 2 (VMF2) as opposed to the symmetric version, VMF1. They then applied VMF2 mapping functions to a very long baseline interferometry (VLBI) experiment and found improvements in baseline length repeatabilities compared to a solution where the symmetric VMF1 mapping functions were used along with a planar gradient parameter estimation. In other words, the use of azimuth-dependent mapping functions not only removes the need for estimating additional gradient parameters in the geodetic analyses but also provides a more accurate representation of the azimuthal variability of tropospheric refractivity compared to the planar surface described by the classic *Chen and Herring* [1997] gradient model. However, VMF2 mapping functions require the derivation of 12 hydrostatic and wet coefficients per site per epoch (for 12 azimuthal nodes of 30°). This requires a much higher computational burden to perform the ray tracing, compared to the derivation of only one hydrostatic and wet coefficient for VMF1 mapping functions. As of today, the authors are not aware of the VMF2 coefficients being available in global grids for use in operational geodetic analyses. In another approach, *Gegout et al.* [2011] introduced Adaptive Mapping Functions (AMFs) to azimuthal anisotropy of the troposphere, which are based on *Marini* [1972] mapping functions of continued fraction form with the addition of a set of Fourier terms for azimuthal dependency of the tropospheric delay. They evaluated the choice of the number of Fourier terms as well as the truncation number of Marini's continued fraction form by fitting adaptive mapping functions using several choices of the above parameters to ray traces of Integrated Forecasting System of ECMWF and studied the residuals of the delays. The best selection among the range of choices for their mapping functions was the AMF with three fractions and four Fourier terms (requiring a total of 27 coefficients), which resulted in accuracies of almost 1 mm for the delays. *Gegout et al.* [2011] also showed that while the hydrostatic component is the largest part of the tropospheric delay, the nonhydrostatic part is the main contributor to the azimuthal heterogeneities of the delay, contributing about 90%. This means that the delays estimated due to horizontal gradients of the troposphere could be mainly related to changes in water vapor at tropospheric altitudes. It should be noted, however, that during particular weather conditions, such as deep convection during high precipitating events, there may be large hydrostatic gradients [*Champollion et al.*, 2004]. *Landskron et al.* [2015] also derived higher-order terms of gradient parameters from ray-traced tropospheric delays and used the extended gradients a priori in their VLBI experiment (however, still using the standard planar gradient model in the VLBI solution). This yielded slightly improved mean baseline length repeatabilities for their experiment and reduced repeatabilities for 65% of the sites when compared to not using any a priori gradient. The scatter improvements were larger when they did not attempt to estimate gradient residuals in the VLBI solution. *Eriksson et al.* [2014] used ray-traced delays from Goddard Earth Observing System version 5 weather model to directly determine asymmetric mapping functions for each quasar observation in a VLBI analysis and discovered improvements in position repeatabilities for about two thirds of the stations in their experiment. In the Global Navigation Satellite System (GNSS) field, *Hobiger et al.* [2008] used ray-traced delays from a mesoscale model a priori in a GPS analysis and realized that the use of these a priori slant delays, together with the estimation of linear gradient residuals, resulted in improved height repeatabilities for most of the sites (by 3% on average), but only slightly improved the horizontal scatters.

A common limitation of the above approaches is that they all rely on ray tracing through a numerical weather model, which may lead to unrealistic delays when the model fails to produce accurate refractivity profiles. Moreover, complications are added in using such techniques in terms of the required amount of computational time and disk storage, which makes them difficult to apply operationally in GNSS analyses. Therefore, an NWM-independent, easy-to-implement technique for modeling the gradients (rather than using a priori information from external sources) might be a more practical alternative for operational GNSS analyses. We have developed a directional gradient model in which tropospheric horizontal gradients are estimated toward

several azimuthal directions around the site, as opposed to the conventional technique where there are only north-south and east-west gradients estimated. This way, we are able to distinguish between different rates of horizontal changes of refractivity at different azimuths around the site.

This paper describes the new directional gradient model, its application for studying specific weather events, and its impact on the estimation of position and zenith total delay parameters. In section 2 we present a more detailed description of the directional model of the gradients. In section 3, we evaluate the capability of the new model to recover simulated gradients at normal and complicated scenarios in comparison with conventional planar model. We also assess the impact of the new model on position and ZTD estimates. In section 4, we apply the new model to an interesting case study of an extreme precipitation event in southern France [Champollion *et al.*, 2004] and look at how the model can help better understand local variabilities of the water vapor field. A second case study is performed in section 5 where skewed time series of a set of Plate Boundary Observatory (PBO) GPS sites in the Sierra Nevada region in western United States (noticed by Materna and Herring [2013]) are tested for the directional model of gradients, and the impact on the time series is studied.

## 2. Directional Gradient Model

In GPS analysis, the azimuthally symmetric part of the delay ( $L_{\text{sym}}$ ) is separated into hydrostatic and wet parts, each part being mapped from the zenith direction to the elevation angle of the observation by the use of an elevation-dependent mapping function, as described, e.g., by Davis *et al.* [1985]:

$$L_{\text{sym}}(\epsilon) = L_h^z m_h(\epsilon) + L_w^z m_w(\epsilon) \quad (1)$$

where  $L_h^z$  and  $L_w^z$  are tropospheric delays for the hydrostatic and wet components at zenith direction,  $\epsilon$  is the elevation angle of the observation, and  $m_h(\epsilon)$  and  $m_w(\epsilon)$  are mapping functions for the hydrostatic and wet components. The hydrostatic part is usually fixed to an a priori value [e.g., Böhm *et al.*, 2006b], and the zenith wet delay is estimated together with other estimation parameters in a least squares solution. An extensive study has been carried out by Tregoning and Watson [2009] on the effect of different tropospheric modeling techniques, including different mapping functions, on position coordinates.

Since it is known that the troposphere is not azimuthally symmetric [e.g., Gardner, 1976; Davis *et al.*, 1993; Gegout *et al.*, 2011], it is also necessary to model the horizontal heterogeneities of the troposphere, which are disregarded in equation (1). The most commonly used approach for modeling the azimuthal asymmetry of the troposphere is to estimate additional horizontal linear gradient parameters in both the north-south ( $L_{\text{NS}}$ ) and east-west ( $L_{\text{EW}}$ ) directions [Davis *et al.*, 1993]; thus, the formulation for the azimuth-dependent part of the delay ( $L_{\text{az}}$ ) becomes

$$L_{\text{az}}(\epsilon, \alpha) = L_{\text{NS}} m_{\text{az}}(\epsilon) \cos \alpha + L_{\text{EW}} m_{\text{az}}(\epsilon) \sin \alpha \quad (2)$$

where  $\alpha$  is the azimuth angle of the observation and  $m_{\text{az}}$  is the mapping function for gradients. The mapping function that is most widely used by analysts is the one introduced by Chen and Herring [1997]:

$$m_{\text{az}}(\epsilon) = \frac{1}{\sin(\epsilon) \tan(\epsilon) + C} \quad (3)$$

in which the constant  $C$  was derived to be 0.0031 by fitting the function to a tilted atmosphere model for different elevation angles from 90 to 5° [Herring, 1992]. This mapping function is preferable over the  $\cot(\epsilon)$  form used, e.g., by MacMillan [1995], which approaches infinity at zero elevation angle, and is not therefore applicable at very low elevations.

The gradient model of equation (2) is based on the idea of estimating a linear gradient and assumes that the refractivity values change linearly from one azimuthal direction of the site toward the opposite direction. In other words, tropospheric refractivity field is considered as a tilted plane. This is a good approximation in normal atmospheric conditions, but a more complicated model might be a better representative of spatial changes in refractivity in cases where there are isolated gradients at specific azimuth angles around the site. Our proposed directional model estimates gradients at discrete user-defined azimuth angles or nodes, using a piecewise function to relate neighboring nodes to one another; therefore, the equation for the azimuth-dependent part of the tropospheric delay for our model becomes

$$L_{\text{az}}(\epsilon, \alpha) = \sum_{j=1}^N L_j m_{\text{az}}(\epsilon) m'_{\text{PW}}(\alpha) \quad (4)$$

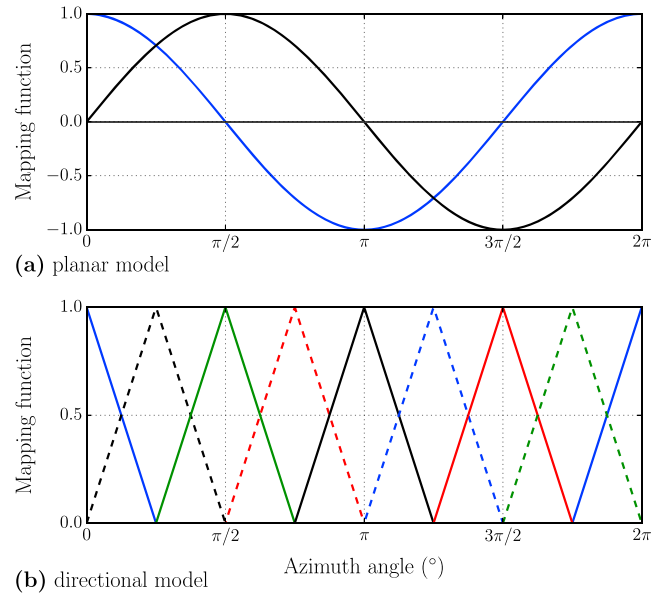


**Figure 1.** The azimuth-dependent mapping functions for (a) conventional planar model of gradients (equation (2)) and (b) directional gradient model with eight gradient parameters. Different colors/line styles show the mapping functions for different gradient parameters.

where  $j$  is the number of nodes at which the gradients are estimated and  $m_{PW}^j(\alpha)$  is a piecewise function based on the azimuth angle of each observation. The piecewise function is defined such that each observation contributes to the estimate of the gradient at two neighboring azimuthal nodes, where the level of contribution depends linearly on the angular distance between observation direction and the direction of the estimated directional node azimuth:

$$\begin{aligned}
 &\text{for } j = 1 : \\
 &m_{PW}^j(\alpha) = \begin{cases} \frac{\alpha - (2\pi - \alpha^*)}{\alpha^*}, & \text{if } \alpha > 2\pi - \alpha^* \\ \frac{\alpha^* - \alpha}{\alpha^*}, & \text{if } \alpha < \alpha^* \\ 0, & \text{otherwise} \end{cases} \\
 &\text{for } 2 \leq j \leq N : \\
 &m_{PW}^j(\alpha) = \begin{cases} \frac{\alpha - (j-2)\alpha^*}{\alpha^*}, & \text{if } (j-2)\alpha^* < \alpha \leq (j-1)\alpha^* \\ \frac{j\alpha^* - \alpha}{\alpha^*}, & \text{if } (j-1)\alpha^* < \alpha \leq j\alpha^* \\ 0, & \text{otherwise} \end{cases} \tag{5}
 \end{aligned}$$

where  $\alpha^* = 2\pi/N$  is the azimuthal grid spacing at which the gradients are estimated. The azimuth-dependent mapping functions for both conventional planar model and directional model are displayed in Figure 1.

The same mapping function described in equation (3) is used in our directional model for mapping the elevation-dependent part of the gradients at each directional node to the zenith direction. We implemented the new model of directional gradients by modifying the GAMIT software [Herring et al., 2015] and then assessed the capability of the model to recover specific cases of gradients using a set of simulations, which are presented in the following section.

### 3. Simulations

To evaluate the capability of the proposed directional gradient model to recover tropospheric properties under a range of conditions, and to evaluate the directional model's impact on other estimated parameters in GPS least squares solution, we analyzed simulated GPS observations using GAMIT software for several different tropospheric gradient scenarios. The station geometry was defined by a set of eight existing permanent

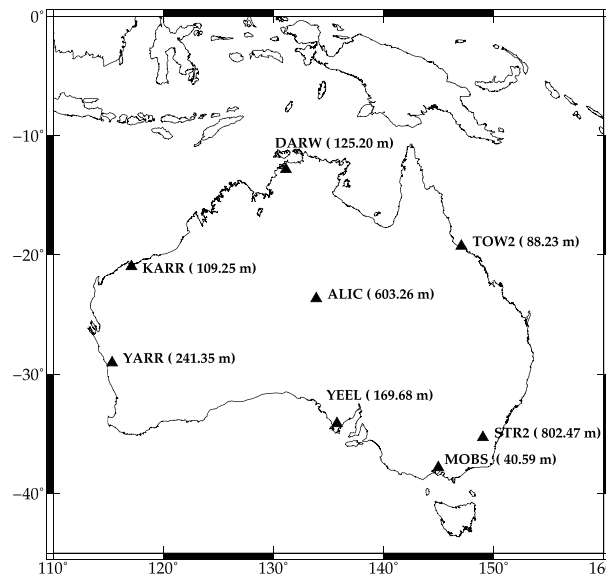


**Figure 2.** The selected network for performing the simulations. The station heights are given in the brackets next to the site names.

GPS stations spanning the Australian continent (shown in Figure 2). We used the actual GPS constellation observation geometry for these sites on the 16 July 2010, simulating the GPS phase and pseudorange observations using the set of models and parameters shown in Table 1.

We did not add any random noise to the simulated signals so that we could investigate the expected (i.e., noise realization-independent) errors in the estimated parameters. In other words, we study how an error in the modeling of the tropospheric horizontal gradient propagates into different estimated parameters.

In our simulations, the troposphere is modeled as fully symmetric (i.e., no tropospheric gradients) for all sites except ALIC, where modeled gradients persist for the entire day. Two different gradient scenarios are presented for ALIC: (A) a simple planar and symmetric gradient scheme toward the northeast of the site (using equation (2) for the full-sky coverage around the station), i.e., positive gradients toward the northeast,

Model/Parameter	Setting
Orbits	IGS final orbits (fixed) [Dow et al., 2009]
Zenith delay estimation interval	2 h
Zenith delay a priori Source	VMF1 for ZHD; GPT + Saastamoinen [1972] for ZWD (ZWD residuals still estimated)
Zenith delay constraints on daily mean value	0.5 m
Zenith delay point-to-point variance	0.02 m/ $\sqrt{h}$
Zenith delay correlation time	100 h
Zenith delay mapping functions	VMF1 for both hydrostatic and wet parts
Gradient estimation interval	6 h
Gradient constraints on daily mean value	0.03 m
Gradient point-to-point variance	0.01 m/ $\sqrt{h}$
Gradient correlation time	100 h
Ocean Loading Earth Tide model	FES2004 [Lyard et al., 2006]
Atmospheric loading	Tidal and nontidal applied at observation level [Tregoning and Watson, 2009]
Antenna phase variations	igs08.atx [Schmid et al., 2016]
A priori coordinates	ITRF2008 [Altamimi et al., 2011]

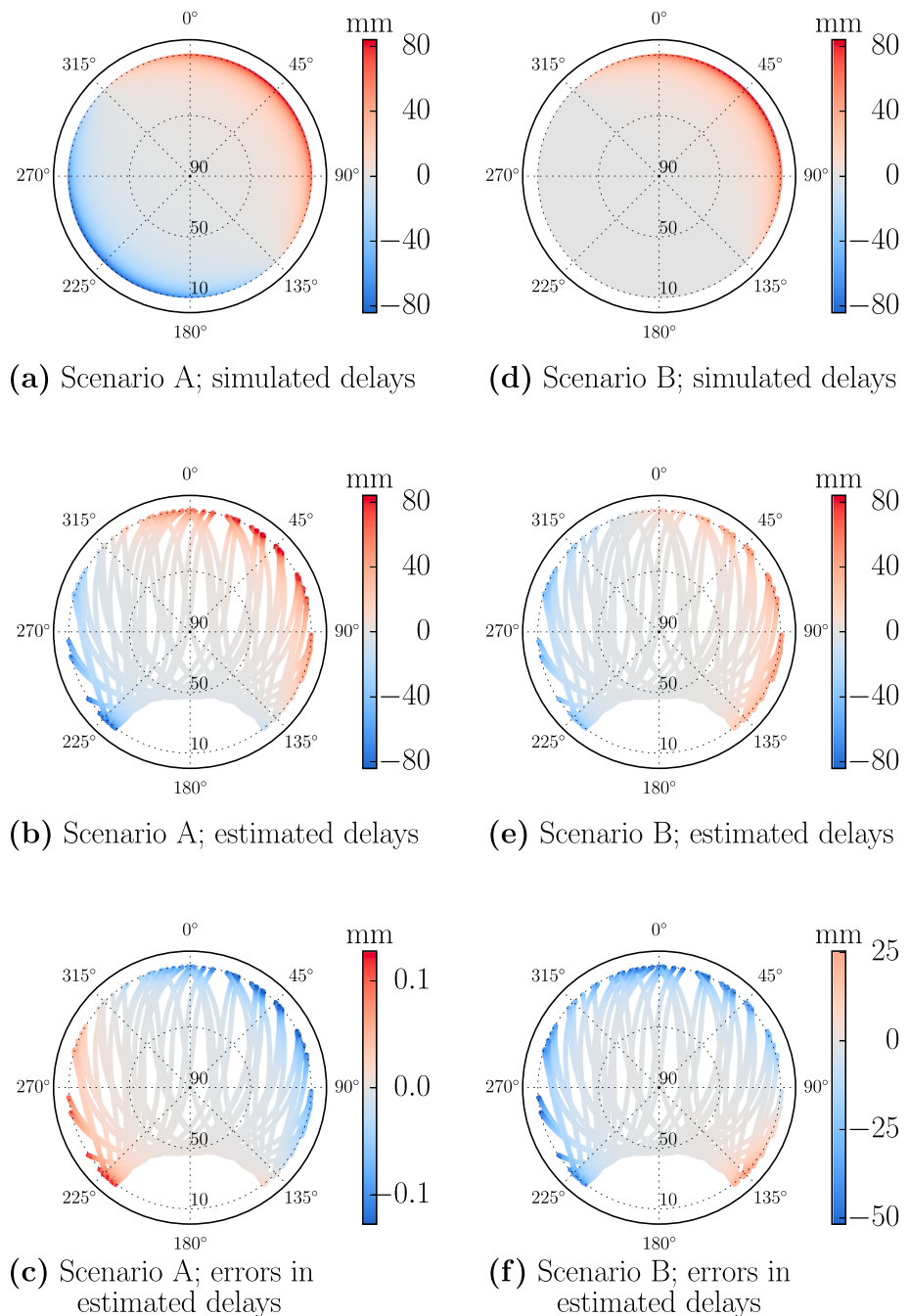


**Figure 3.** The slant delays due to the two different simulated scenarios of tropospheric gradients and the estimated delays using the planar model of gradients at site ALIC. (a) Simulated scenario A. (b) Estimated delays for scenario A. (c) Errors in the estimation of delays for scenario A. (d) Simulated scenario B. (e) Estimated delays for scenario B. (f) Errors in the estimation of delays for scenario B. Note the change in scale for Figures 3c and 3f. The 1-sigma uncertainty on the maximum error in Figure 3f is  $\sim 5$  mm.

and negative gradients toward the southwest (Figure 3a), and (B) an asymmetric gradient scheme only toward the northeast, with no gradient when looking to the southwest of the station (Figure 3d). For the second scenario, we still use equation (2) but apply it only for the half of the sky coverage in the azimuth range of  $-\pi/4$  to  $3\pi/4$  (we apply zero gradients for the rest of the sky coverage). We use the letters A and B, and the terms symmetric and asymmetric gradients, from this point on to refer to the two different gradient scenarios described above. We then try to recover the simulated gradients as well as station positions and zenith total delays



by solving the least squares problem using both the conventional planar and directional models of gradients. Except for the gradient model, we use the same models and parameters for both solutions (Table 1).

In the following subsections, we show the effect of (1) the conventional planar gradient parametrization and (2) the directional gradient parametrization on GPS solutions for both A and B simulated gradient scenarios. We also assess how the inclusion of observations at different elevation angles impacts the misfit of the gradients using an elevation cutoff sensitivity test. We then investigate the effect of mismodeling in the tropospheric gradients on different estimated parameters and how the directional model could reduce these errors. A discussion of the correlations between estimated parameters in these different solutions then follows. Finally, we discuss the number of directional gradient estimation nodes and its impact on the solutions.

### 3.1. Recovering Simulated Gradients Using Planar Model Parametrization

In this section, we present the results of the estimation of tropospheric gradients using the planar gradient model parametrization for the two simulated observation scenarios A and B.

#### 3.1.1. Scenario A—Symmetric Gradients

The estimated planar tropospheric gradient delays for scenario A are displayed in Figure 3b. An elevation cutoff angle of  $10^\circ$  has been arbitrarily chosen for the solutions in Figure 3 as this is a commonly used cutoff for geodetic analyses. In these solutions, the position components are estimated along with tropospheric zenith total delays and gradient parameters. In this normal symmetric gradient scenario (scenario A; Figure 3a), the conventional planar model is able to fully recover the simulated gradients with errors of almost zero (Figure 3c).

#### 3.1.2. Scenario B—Asymmetric Gradients

While the planar gradient model performed well in the simple symmetric gradient simulation scenario, it only partially recovers the gradients for the more complicated asymmetric gradient scheme of scenario B (Figure 3d). The planar model seriously underestimates the positive gradient delay in the northeast direction and estimates an erroneous negative gradient delay in the southwest direction, as well as a positive gradient delay in the southeast direction, where the gradients, in fact, should be zero (Figure 3e). As seen in Figure 3f, the errors reach values of larger than 50 mm at  $10^\circ$  elevation angle, which is well above the 1-sigma uncertainty level of the relevant gradient estimate ( $\sim 5$  mm), and easily exceeds a 3-sigma rule of thumb for statistical significance.

### 3.2. Recovering Simulated Gradients Using Directional Model Parametrization

#### 3.2.1. Scenario A—Symmetric Gradients

Figure 4 shows the delays due to gradients when a directional model parametrization, with gradients estimated every  $45^\circ$  in azimuth, is implemented. For the symmetric simulated scenario A (Figure 4a), we are still able to recover the planar gradients well, although with slightly poorer accuracy than with the planar model (see Figures 4b and 4c). We observed errors of up to  $\sim 7.5$  mm for the gradient-induced delays at  $10^\circ$  elevation. This error occurs most likely because we are using a different gradient model to estimate the horizontal gradients (the directional model of equation (4)) than the model we used to simulate the gradient delays in the observations (the planar model of equation (2)).

#### 3.2.2. Scenario B—Asymmetric Gradients

The directional gradient parametrization shows its superiority over the planar model in the asymmetric simulated scenario B (Figure 4d). Unlike the planar model (Figures 3e and 3f), the directional approach (Figure 4e) retains the original simulated shape of the troposphere (positive gradients toward the northeast and zero gradients toward the opposite direction). The errors in delays caused by gradients for this solution at  $10^\circ$  reach a maximum of only about 6 mm (Figure 4f) with a 1-sigma uncertainty of  $\sim 12$  mm. This is significantly smaller than the  $\sim 50 \pm 5$  mm errors for this scenario using the planar model. The uncertainties, however, grow when using the directional model, which is a result of having more parameters in the least squares inversion. It should be noted that the directional model with  $45^\circ$  azimuthal nodes for the estimation of gradients requires eight gradient parameters per site per epoch, while the planar model only needs two parameters per site per epoch.

### 3.3. Elevation Cutoff Sensitivity of the Gradient Misfits

The results shown in Figures 3 and 4 are generated using a  $10^\circ$  elevation cutoff angle. However, the tropospheric horizontal gradients are largest at the lowest elevation angles. Although most geodetic analyses are currently performed using  $10^\circ$  elevation cutoff angles, studies aimed at tropospheric estimations suggest that using lower elevation observations increases the sensitivity of the solutions to the tropospheric zenith

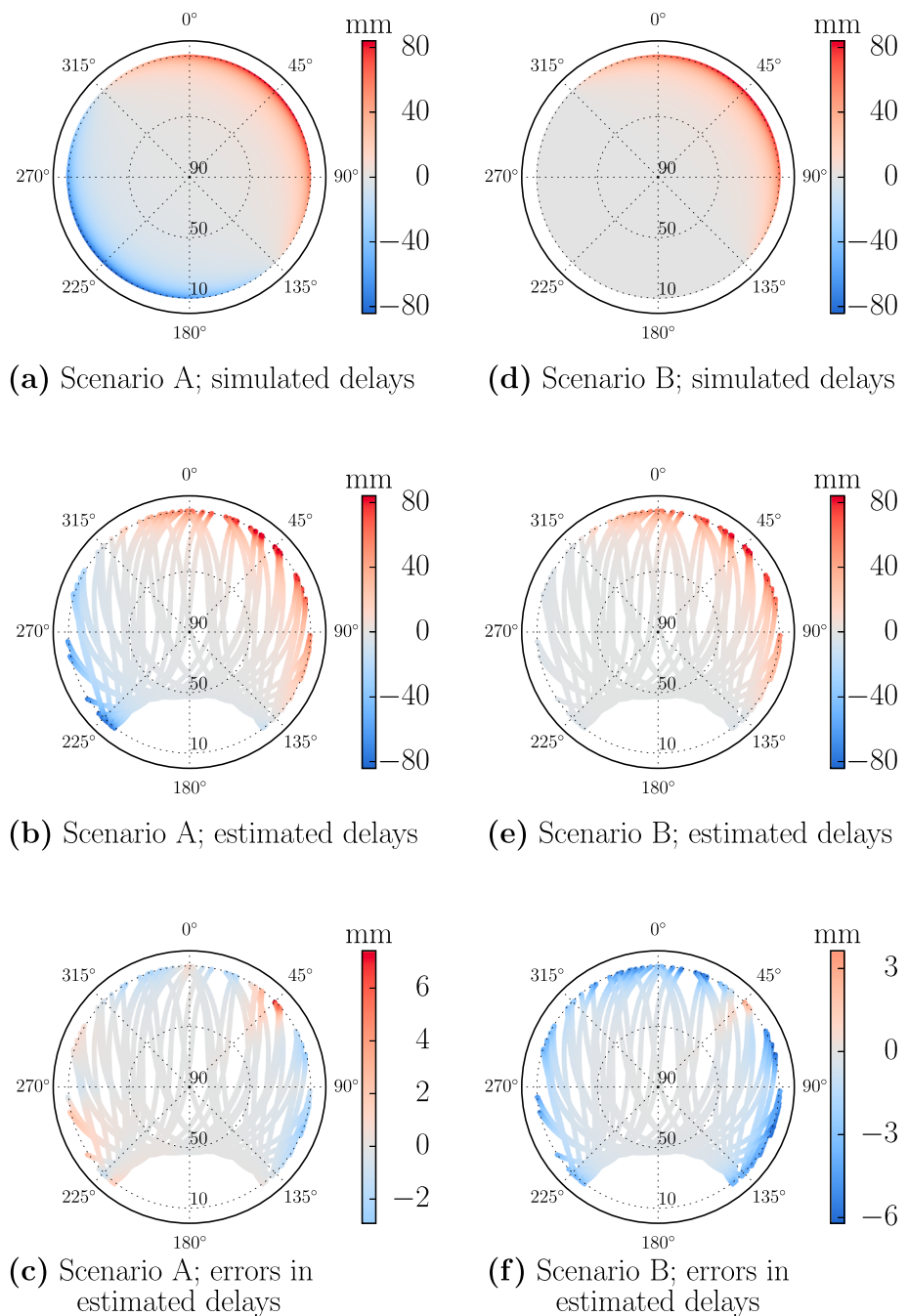


**Figure 4.** The slant delays due to the two different simulated scenarios of tropospheric gradients and the estimated delays using the directional model of gradients at site ALIC. (a) Simulated scenario A. (b) Estimated delays for scenario A. (c) Errors in the estimation of delays for scenario A. (d) Simulated scenario B. (e) Estimated delays for scenario B. (f) Errors in the estimation of delays for scenario B. Note the change in scale for Figures 4c and 4f. The 1-sigma uncertainty on the maximum error in Figure 4f is  $\sim 12$  mm.

delays/precipitable water [e.g., *Tregoning et al.*, 1998]. Therefore, it is recommended for GPS meteorology applications to include low-elevation observations in the analyses, as long as mapping function errors and local site-specific errors allow for accurate estimation of tropospheric parameters.

We performed the analysis for different choices of elevation cutoff angle (from  $20^\circ$  to  $3^\circ$ ) and calculated the misfit in the tropospheric horizontal gradients. Figure 5 shows the gradient misfit as a function of the



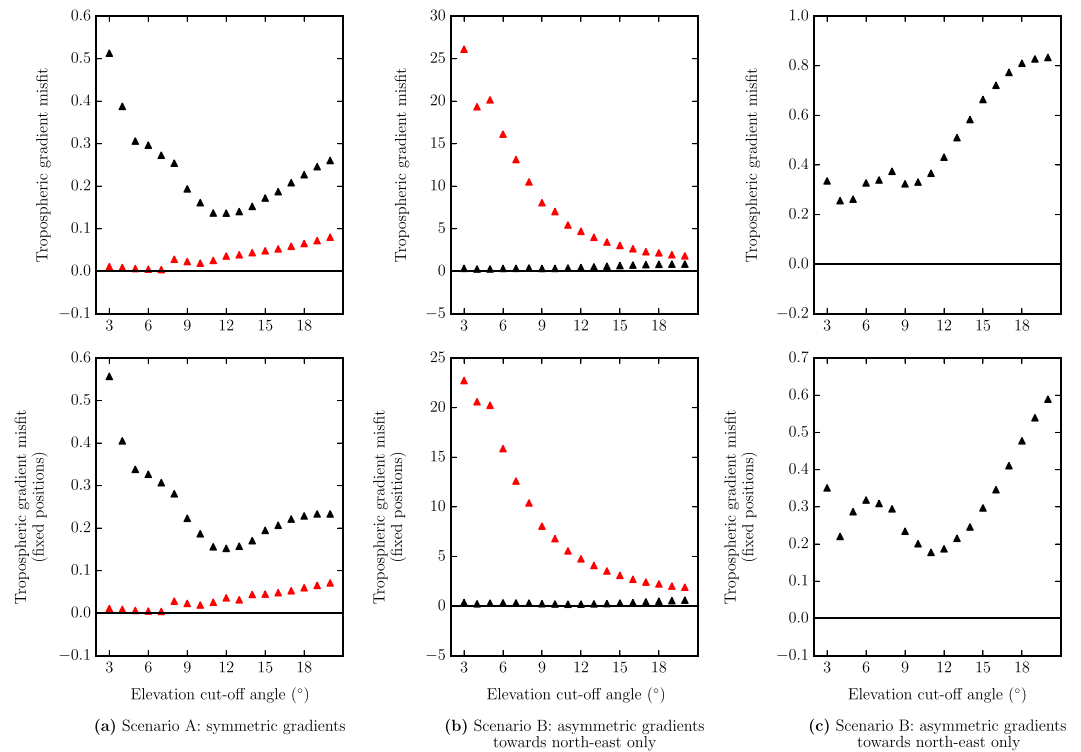


**Figure 5.** Tropospheric gradient misfit as a function of elevation cutoff angle for (a) symmetric gradient simulation scenario A and (b and c) asymmetric gradient simulation scenario B. Red triangles show the misfits when using the planar gradient model, and black triangles depict the misfits when using the directional model of gradients. Figure 5c is the same as Figure 5b but only displaying the misfits when using the directional model of gradients, to avoid the scale difference between the two models. The top plots are the misfits when the position components are estimated along with other parameters, and the bottom plots are the results from fixing the positions to their true values and only estimating tropospheric zenith delays and gradients.

elevation cutoff angle set in the GPS processing for both the symmetric and asymmetric gradient simulation scenarios A and B using both planar and directional models. For each analysis, we calculated the misfit ( $\delta$ ) in the tropospheric horizontal gradients according to

$$\delta = \sqrt{\frac{1}{N} \sum_{i=1}^N \left[ \left( \frac{\hat{l}_i - l_i^t}{\sigma_i} \right)^2 \right]} \quad (6)$$

where  $\hat{l}_i$  is the estimated gradient delay for the  $i$ th observation in the day,  $l_i^t$  is the corresponding true simulated gradient delay,  $\sigma_i$  is the 1-sigma uncertainty of the estimated gradient delay, and  $N$  is the number of observations for the whole day. Ideally, the misfit values should be zero, since there is no random noise added to the simulations, and the estimated gradient delays should be identical to the true gradient delays.

Figure 5 shows the gradient misfit for different choices of the elevation cutoff angle. Looking at Figure 5a for the symmetric simulated scenario A, the misfits in the tropospheric gradients using the planar model are almost zero at elevation cutoff angles below  $8^\circ$  and reaches about 0.1 at  $20^\circ$  cutoff. The directional model results in larger misfits at all elevation angles, but the misfits are still under 0.6. This higher misfit was also evident in Figure 4 and is a result of the differences between the models used for simulation and estimation of the tropospheric gradients.

For the asymmetric gradient scenario B (Figure 5b), the planar gradient model clearly results in large misfits up to about 25, whether we put loose constraints on the positions or fixing them to their true values. The misfit is largest when low-elevation observations are included. This is an important outcome of this study: while it could be useful for tropospheric studies to include low-elevation observations, one has to consider the

fact that in asymmetric gradient situations the planar model of the gradient is unable to properly model the horizontal changes of the tropospheric refractivity, and the addition of low-elevation observations actually degrades the solution.

The directional model, on the other hand, yields very small misfits of below  $\sim 0.8$  at all elevation cutoff angles, which is the result of a better parametrization of the gradients for this asymmetric condition, and shows that the directional gradient model is an improvement on the conventional planar model in the asymmetric gradient conditions.

Figure 5c displays only the gradient misfits from using the directional model to more clearly show the changes of the misfits with elevation cutoff. There is a general increase in gradient misfits when lower elevation observations are excluded from the analyses, which indicates that the low-elevation observations can help the directional model to better resolve the gradients. Also, fixing the positions helps to reduce the level of gradient misfits (e.g., from  $\sim 0.3$  to  $\sim 0.2$  at  $10^\circ$  cutoff). There is, however, a small fluctuation in the gradient misfit at elevation angles below  $10^\circ$ , but to make a conclusion on whether this small increase in the gradient misfit is more harming than benefiting the solutions, it is important to also examine how the other derived parameters are impacted at these very low elevation cutoff angles. The impact on other parameters is discussed in the next section.

### 3.4. Impact on Derived Parameters

For the analyses performed in section 3.3, we also calculated the errors (estimated minus true values) in position and ZTD parameters. These biases are displayed in Figure 6 for different estimated parameters. It is evident from Figure 6a that under a normal symmetric gradient scenario with no data noise, both planar and directional gradient models estimate error-free parameters. The directional model, however, yields larger uncertainties (particularly as the elevation cutoff increases). These larger uncertainties could be reasonably attributed to the higher number of parameters and are reduced for the ZTD estimates by removing the position components from the set of parameters to be estimated. Nevertheless, the small misfits in the tropospheric gradients when implementing the directional gradient model under symmetric scenario (seen in Figure 4c) do not yield any significant bias in the estimates of position and ZTD parameters.

Under the asymmetric gradient scenario (Figure 6b), the directional model clearly outperforms the planar model in the estimation of all parameters at elevation cutoff angles below  $10^\circ$ . The mismodeling of the tropospheric gradients by the planar model in this scenario results in errors in position and ZTD parameters, particularly when including low-elevation measurements. Latitude estimates by the planar model contain errors of up to about 1.5 mm at  $3^\circ$  cutoff, and longitudes are erroneous by about 1 mm at the same cutoff. The impact on the height and ZTD estimates are much larger: the errors reach about 10 mm for height and 6 mm for ZTD at  $10^\circ$  cutoff and close to 20 mm for height and 10 mm for ZTD when including very low-elevation observations (down to  $3^\circ$ ) in the solution. The significant growth of errors in parameters caused by the planar gradient model when decreasing the elevation cutoff angle stems from the fact that the contribution of horizontal gradients is largest at low elevations; therefore, a more accurate representation of the gradients becomes more important when including low-elevation observations in the analysis of GPS data.

The more accurate representation of the tropospheric gradients of the asymmetric scenario B by the directional model resulted in improvements from the planar model for the estimation of all parameters (Figure 6b; black triangles). Unlike the planar model, the directional model enables the use of data down to very low elevation angles ( $3^\circ$ ) without introducing any error into any of the estimated parameters, which is a direct result of a much more accurate representation of the tropospheric gradients by the directional model as seen by better misfit of the gradients as observed in Figures 4 and 5. The uncertainties on the estimated parameters are larger than those generated by the planar model, as is expected by the higher number of parameters in the directional parametrization.

When setting higher-elevation cutoff angles and using the directional gradient model, biases are introduced into height and ZTD parameters in the asymmetric gradient scenario. A higher misfit was also previously observed in the gradients (Figure 5c) for the same scenario when using higher cutoff angles. Both the gradient misfits and the errors in ZTD estimates, as well as their uncertainties, are reduced when fixing the positions to their true values. The fact that the use of low-elevation observations and/or fixing the position parameters to their true values yields more accurate estimates of the derived parameters indicates that these errors could be caused by possible high correlations between the parameters when using the directional model of

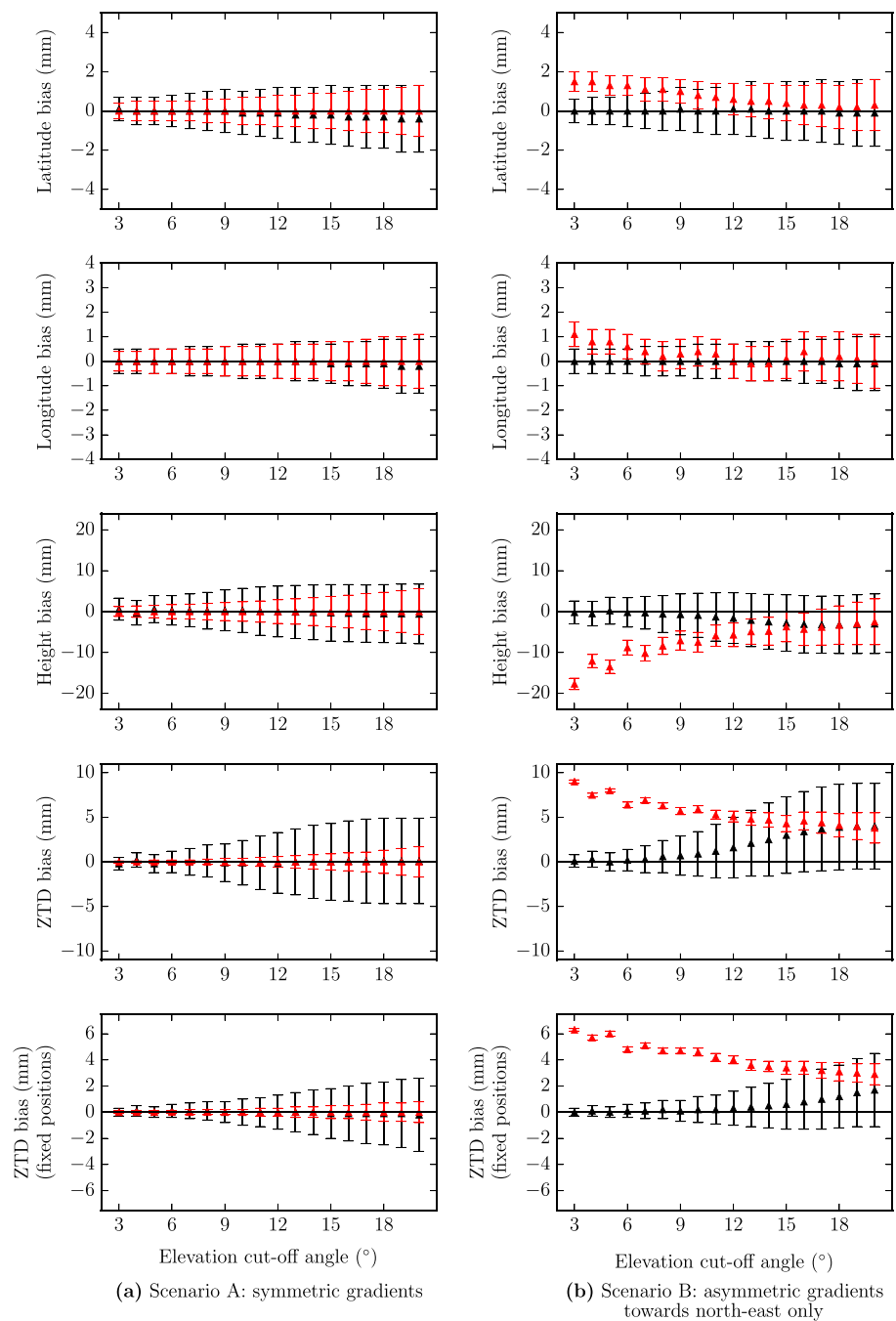


**Figure 6.** Biases in the estimation of different parameters at site ALIC using conventional planar gradient model (red) and new directional gradient model (black) for (a) the simulated scenario A and (b) the simulated scenario B. The errors shown for ZTD are the biases for daily mean values of zenith total delay. The error bars are the 1-sigma uncertainty of the estimates.

gradients in the least squares inversion. In the absence of noise, however, the estimates should contain zero errors, despite any correlations between the parameters. The existence of errors can therefore also be attributed to the different model we use to estimate the tropospheric horizontal gradients (equation (4)) compared to the model we used to simulate the gradients (equation (2) with a constraint to generate only a half-sky gradient to the northeast). Possible correlations between the parameters when using the directional gradient model and the slightly different models for simulation and regression are probably the main drivers for the estimation errors; it is therefore worthwhile at this stage to inspect the correlation coefficients between the estimated parameters.

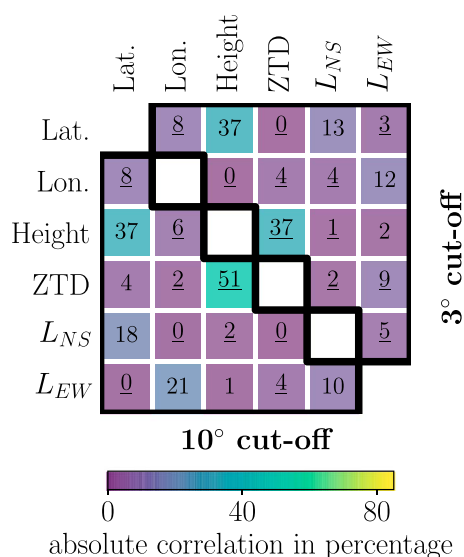


**Figure 7.** Correlations between different estimated parameters at site ALIC for simulation scenario B when using the conventional planar model of gradients at 10° cutoff (lower triangle) and 3° cutoff (upper triangle). The correlation coefficients are also displayed in percentage terms on each matrix element; the underscored numbers show negative correlations.

is slightly reduced when including low-elevation observations in the solution (from  $-0.51$  to  $-0.37$ ). There are also correlations between height and latitude parameters (0.37). North-south and east-west gradient parameters are not correlated with height/ZTD nor with each other. Looking at Figure 8, on the other hand, suggests that the directional gradient parameters are highly correlated with heights, zenith delays,

### 3.5. Correlations

Correlation coefficients between the estimated parameters are displayed for site ALIC in Figure 7 for the planar model and in Figure 8 for the directional model. Correlations are displayed for the 10° and 3° cutoff solutions to study the impact of low-elevation observations. We show correlations of the 10° cutoff solutions in the lower triangular matrices and the correlations of the 3° cutoff solutions in the upper triangular matrices, and we put the two triangular matrices in the same figures to make the comparisons between high and low cutoff angles easier. The correlations are shown in absolute percentage terms. These absolute correlation percentages are also displayed as numbers on each matrix element, and the negative correlations are depicted as underscored numbers.

The well-known existence of high correlations between heights and zenith delays [e.g., Rothacher and Beutler, 1998] is evident from Figure 7 (lower triangle); this correlation

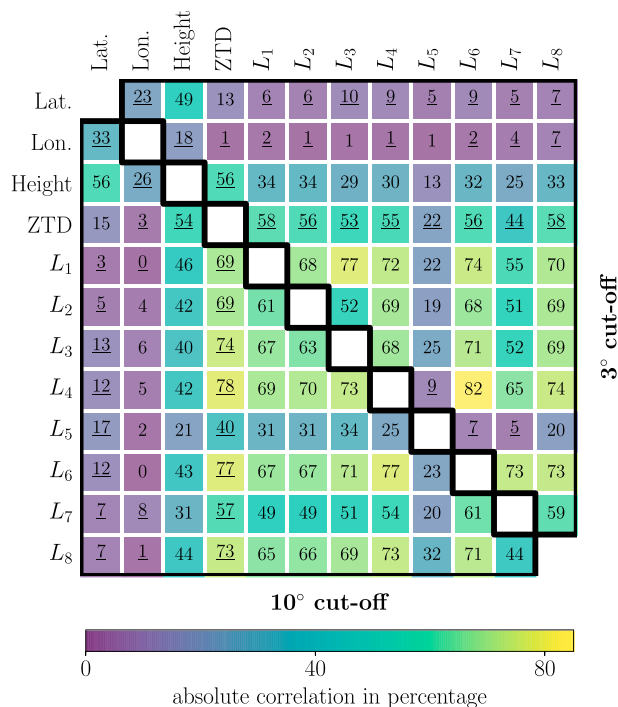


**Figure 8.** Correlations between different estimated parameters at site ALIC for simulation scenario B when using the directional model of gradients at 10° cutoff (lower triangle) and 3° cutoff (upper triangle). The correlation coefficients are also displayed in percentage terms on each matrix element; the underscored numbers show negative correlations.

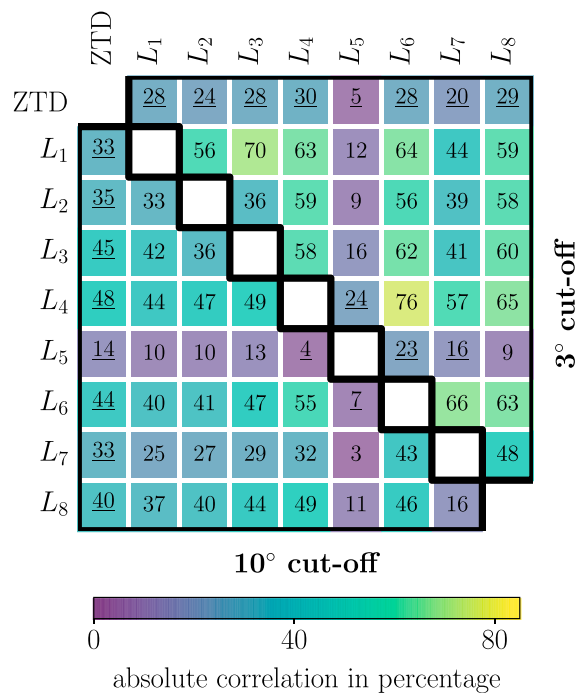


**Figure 9.** Correlations between different estimated parameters at site ALIC for simulation scenario B when using the directional model of gradients and fixing position components to their true values at 10° cutoff (lower triangle) and 3° cutoff (upper triangle). The correlation coefficients are also displayed in percentage terms on each matrix element; the underscored numbers show negative correlations.

to the order of ~0.4 at 10° cutoff. These correlations are further reduced to the order of ~0.25 when also including low-elevation measurements (and fixing the positions). Correlation levels between the gradient parameters themselves are also reduced when fixing the positions, either using a 10° or a 3° cutoff. The reduction in ZTD/gradient correlations appears as almost zero estimation errors of ZTD when tightly constraining positions to their known values (Figure 6b and the relevant discussion in section 3.4).

The investigation of the correlation coefficients between different estimated parameters showed that the high correlations between the new tropospheric gradient parameters and height/ZTD parameters could be mitigated by including low-elevation observations and/or putting tight constraints on position parameters. This will lead to reduced errors in the estimation of height and ZTD parameters by either including low-elevation measurements or fixing the position parameters as seen in Figure 6b. The correlations between different directional gradient parameters are also reduced when fixing the position components but do not significantly change by setting a cutoff angle lower than 10°. This leads to the gradient misfits being reduced when putting tight constraints on the position parameters, but not by including lower elevation observations than 10° (Figure 5c). The gradient misfits for the asymmetric gradient scenario are significantly smaller using the directional model than given by the planar model (Figure 5b). We also performed a more complete test, deriving correlation coefficients between the important solution parameters as a function of the elevation cutoff angle choice from 20° to 3°. We have provided these results in the supporting information Figure S1. These statistics show how solution parameter correlations change with the choice of elevation cutoff and how these changes are related to changes in the errors of parameter estimates (Figure 6).

### 3.6. Number of the Directional Gradient Parameters

By default in this paper, we estimate eight directional gradient parameters for each station and each epoch, meaning that we set the size of pie wedge sections of the model as 45°. However, one may choose to estimate a different number of directional gradients. A lower number of directional parameters may result in the gradients not being fully captured by the model, while choosing a very high number of directions may result in unnecessary high number of parameters, lower degree of freedom, and higher computational time.

and also with each other. The correlations between gradients and zenith delays are most significant. Including low-elevation observations (upper triangle of Figure 8) reduces the correlations between the gradient and height/ZTD parameters. These reduced correlations are probably one reason for the improved estimation errors of ZTD and height parameters when including low-elevation observations as observed in Figure 6. The between-gradient correlations, however, do not change significantly by including observations lower than 10°, which is consistent with the gradient misfits not changing significantly at elevation cutoff angles below 10° (Figure 5c). Low correlations between the southward gradients (L<sub>5</sub>) and other parameters, seen in Figure 8, are simply because there are no low-elevation observations in this direction.

Another way to mitigate the impact of the correlations is to fix the positions to their known values. The correlations from the fixed-position solutions are shown in Figure 9 in the same way as in Figures 7 and 8. High reductions in the correlations when fixing the positions are evident: ZTD/gradient correlations are reduced from the order of ~0.7

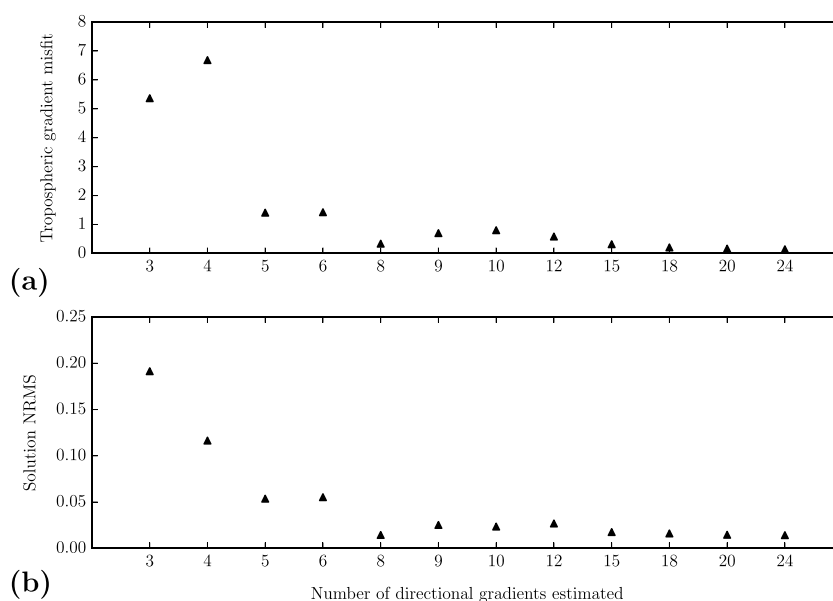


**Figure 10.** (a) The tropospheric horizontal gradient misfit and (b) NRMS of the solution, as a function of the number of directional gradients estimated in the GPS analysis of the simulated asymmetric gradient scenario B.

We performed a series of tests to investigate the resolving power of the directional gradient model, estimating between 3 and 24 directional gradient parameters to recover the simulated asymmetric gradient from simulation scenario B, using a  $3^\circ$  elevation cutoff. For each tested number of directions, we derived the normalized root-mean-square (NRMS) error of the solution as well as the misfit in the tropospheric gradient estimates using equation (6), which are displayed in Figure 10. It is evident from the NRMS and misfit results that estimating three or four directional gradient parameters does not accurately capture the gradient scheme of scenario B, leading to gradient misfits of larger than 5 and solution NRMS values of more than 0.10. Estimating five or six gradient parameters significantly reduces both gradient misfit and NRMS but still results in gradient misfits of larger than 1 and NRMS of higher than 0.05. Once we estimate the eight gradient parameters, the misfit in the gradient and the solution NRMS reach values close to zero ( $\sim 0.3$  for gradient misfit and  $\sim 0.01$  for solution NRMS). By choosing higher number of directional gradients than 8, the misfit does not change significantly. The higher misfit of the four-direction model compared to the three-direction model, as well as the higher misfits of 9-, 10-, and 12-direction models compared to the 8-direction model, is probably related to the azimuthal location of the gradient estimation nodes with respect to the simulated (true) gradient shape. Nonetheless, it is clear from Figure 10 that in order to resolve the gradient shape of the simulated scenario B with sufficient accuracy, estimating at least five gradient parameters is necessary, and estimating eight gradient parameters is sufficient.

To more clearly show the effect of estimating different number of directional parameters, the gradient delay estimates, as well as the errors in the estimates of gradient delays, are displayed in supporting information Figures S2 and S3 as sky plots for the solutions with three, four, five, six, and eight directions. The choice of the number of directional gradients also depends on the shape of the real gradient scheme (which is unknown in practice) and the number of observations available. We performed tests using postfit residuals as an indicator to decide which gradient model (planar or directional/how many directional gradients) should be used for each station and day. However, due to the existing correlations between gradients and other parameters, some parts of the gradient signals are usually absorbed into other parameters, making it difficult to rely on postfit residuals only to extract information about the gradient shape. Thus, a practical methodology for decision on an optimal model which can be relied on at all times remains a limitation of the current work. Nevertheless, using eight directions seems to be an appropriate trade-off among the solutions with different number of directional gradient parameters.



### 3.7. Summary of the Simulation Study

The simulation study carried out in this section shows that the proposed directional model of gradients is able to improve parameter estimates for specific cases when the tropospheric delay horizontal changes do not follow a simple planar model. The largest impacts of mismodeling the gradients in these scenarios are seen on station height and ZTD parameter estimates. In general, while the directional gradient model results in slightly poorer misfits in the tropospheric gradients under normal symmetric gradient scenarios and higher uncertainties on all the estimated parameters (due to larger number of correlated parameters), it outperforms the conventional planar parametrization in abnormal asymmetric gradient situations. In such asymmetric conditions, the directional model allows the use of low-elevation observations and results in improved estimates of height and ZTD compared to the planar model. Both the uncertainties and errors in parameters estimated by the directional model can be reduced by including low-elevation observations and/or fixing or constraining station positions, thus reducing the correlations between gradient and height/ZTD parameters. Estimating eight directional gradient parameters appears to provide the optimum trade-off between the increased resolving capability of the solution and the degree of correlations between parameters.

In the next two sections, we show the impact of using the directional model in two real case studies: the V shape intense precipitation event that occurred in southern France causing flash flooding from heavy rainfall of September 2002 and the skewed position time series of PBO sites in Mammoth Lakes area in California.

## 4. Case Study of the 8–9 September 2002 Torrential Rain Event in Southern France

We have already shown in the simulations of section 3 that the directional model of gradients is able to improve our understanding of the tropospheric gradients (and consequently water vapor) in abnormal weather situations. It is also important to show the capability of the model by evaluating it on real case studies where there are isolated gradients at some directions around a GPS site. A very good example of such cases is the 8–9 September 2002 torrential rain event in southern France. The event was an extreme example of an intense but common Cévenol episode that often impacts the Cévennes area between Massif Central mountains and the Mediterranean Sea in autumn. A Cévenol episode is characterized by an intense upper level cold trough between Ireland and the Iberian Peninsula that produces a low-level south wind flow in the southern France. The warm moist air from the Mediterranean Sea is brought to the coast by this flow, and the topographic effect of the Alps, Pyrenees, and Massif Central Mountains helps to further destabilize the atmosphere above the region [Delrieu *et al.*, 2005]. The particular extreme precipitation event of 8–9 September 2002 was reported to involve one of the highest precipitation amounts and river discharges ever recorded for a large area: the accumulated amount of rainfall during this event was more than 300 mm for a region of about 5000 km<sup>2</sup> over 48 h [Champollion *et al.*, 2004].

Thorough analyses of the 8–9 September flash flood event are performed by, e.g., Delrieu *et al.* [2005], Champollion *et al.* [2004], and Brenot *et al.* [2006]. Figure 11 shows the reanalyzed rainfall maps for this event provided by the Cévennes-Vivarais Mediterranean Hydrometeorological Observatory (CVMHO). The reanalysis maps are derived by merging information from Météo France ARAMIS network of radars and hourly and daily rain gauge measurements operated by Météo France, the Service de Prévision des Crues du Grand Delta, and Electricité de France using a kriging approach with external drift described by Delrieu *et al.* [2014]. A detailed description of the database the rainfall reanalysis data are retrieved from is given by Boudevillain *et al.* [2011].

As for a typical case of Cévenol event, the elongated upper level deep cold trough that formed between Ireland and Iberia on 8 September 2002 resulted in a southerly surface flow around the low-pressure system above the Mediterranean Sea and southeastern France at around 04:00 UTC, bringing the warm moist air from the sea to the Gard region starting from 08:00 UTC (Figure 11b). The tropopause level southwesterly diffluent flow led to the convection being formed as a V shape (Figure 11d), with the maximum precipitation and cloud heights at the edge, and the clouds forming the branches of the V shape along Massif Central mountains. The region of precipitation persisted until the afternoon of 9 September, when the surface winds started weakening (as a result of the trough changing its direction from north-south to northwest-southeast), and the convective system shifted farther east (Figure 11g), marking the end of heavy precipitation event [Delrieu *et al.*, 2005; Champollion *et al.*, 2004].

The GPS station at Montpellier (MTPL) is located very close to the edge of the V shape precipitation pattern, making the site an appropriate test case for the gradient model. We processed GPS data for a network of about

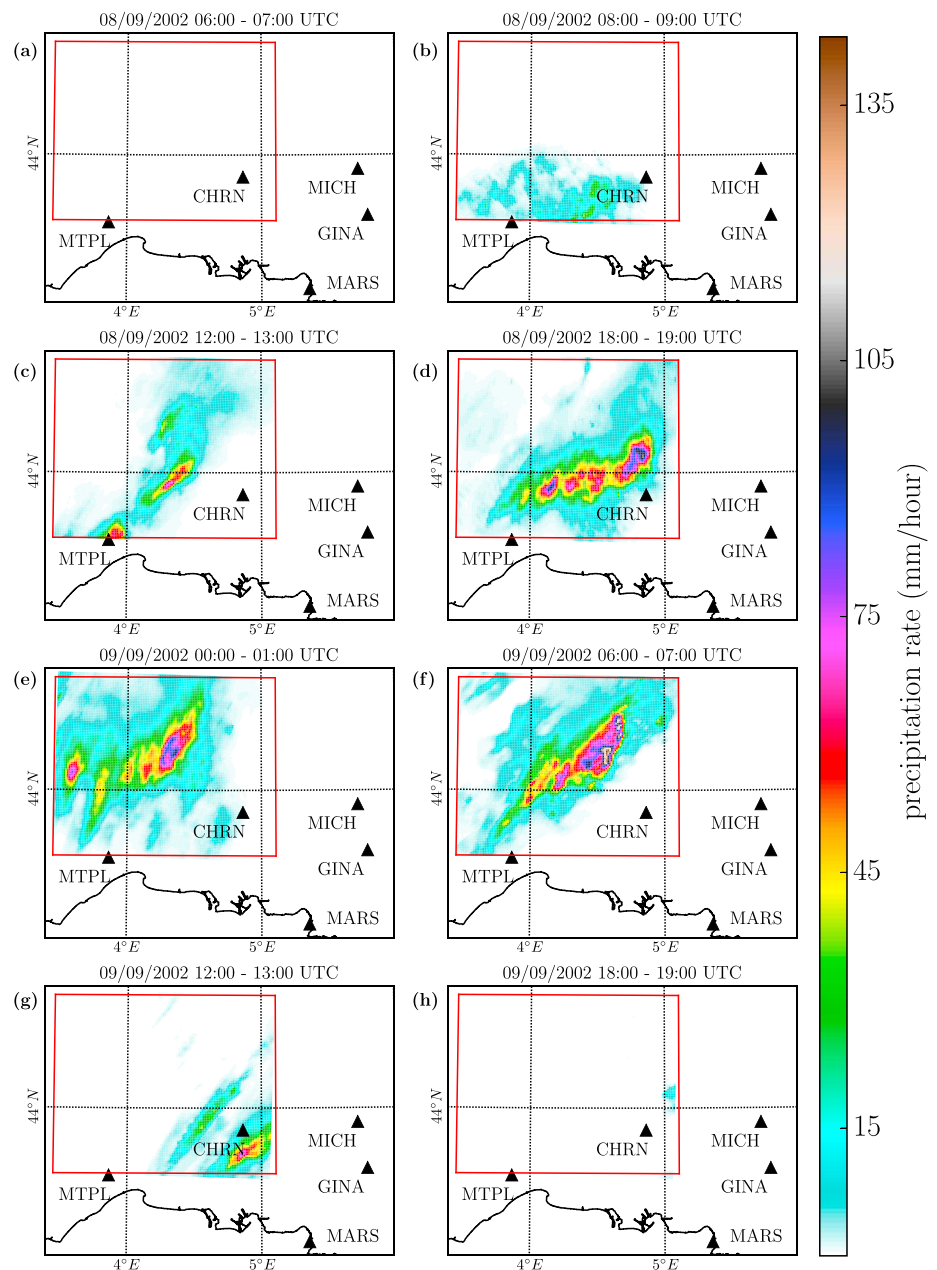


**Figure 11.** Hourly precipitation during the September 2002 event in the Gard region in southern France; the red box is the region where there is krigged data available from CVMHO SEVnOL. Data courtesy of <http://www.ohmcv.fr>.

30 sites well distributed across the European continent, including the sites shown in Figure 11. Two separate solutions were carried out: one with the conventional planar model of gradients and the other with estimating eight directional gradients around each site. We compared slant delays from both gradient models (Figure 12) at the epochs for which there are precipitation values (cf. Figure 11). The empirical site-specific model (ESM) introduced by Moore *et al.* [2014] was applied in both solutions in order to ensure that any site-specific errors, including multipath, were removed from the solutions. We first performed a solution for 1 month of data around the day of interest using the planar model of gradients and other parameters as stated in Table 1, then derived the ESM from the postfit one-way residuals, and finally carried out both planar and directional model solutions while applying the derived ESM to both of them. In addition, for both cases we used the estimated monthly averaged positions a priori and only estimated zenith delay and gradient parameters.

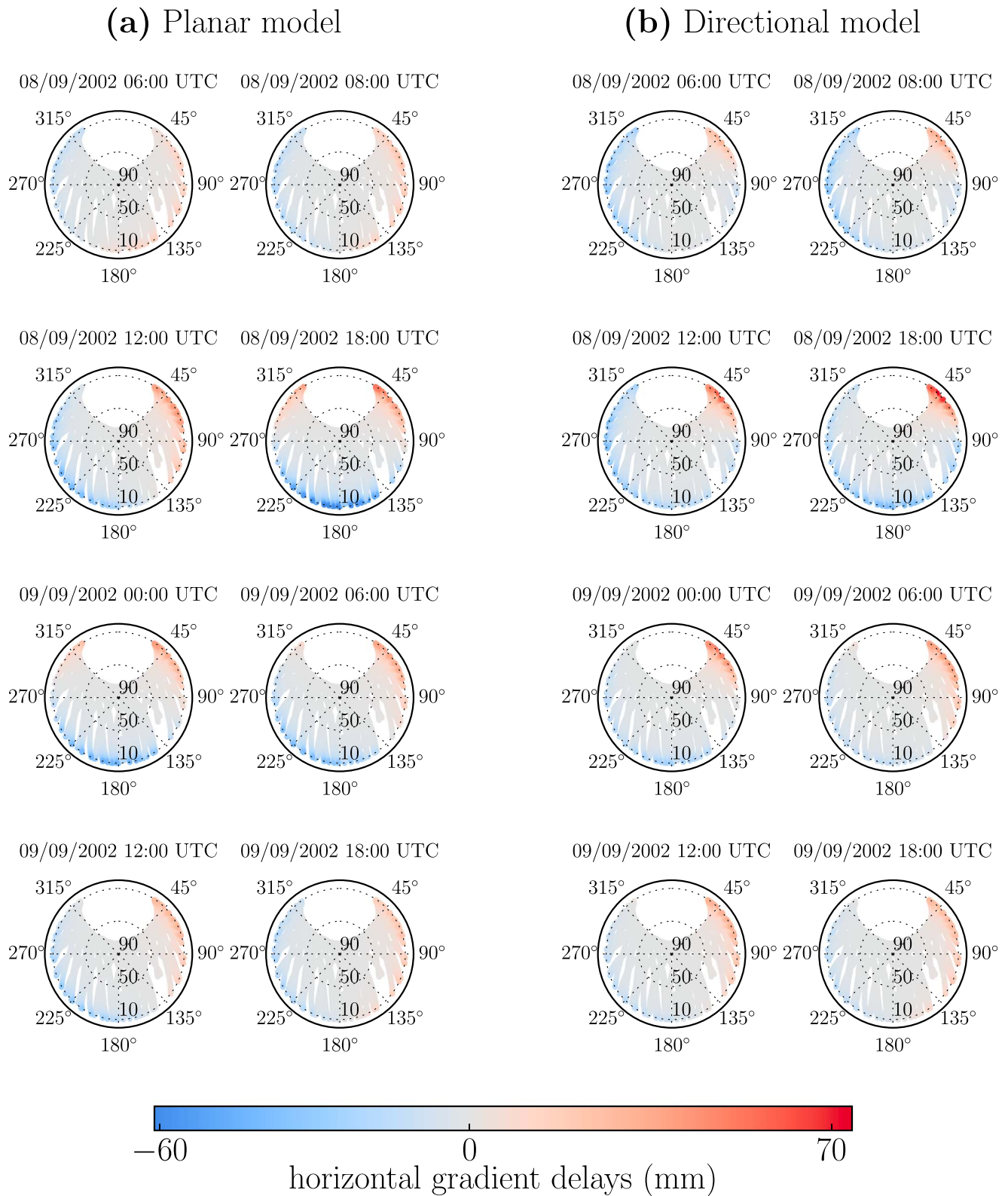


**Figure 12.** Horizontal gradient delays estimated at site MTPL using (a) the conventional planar model and (b) the directional model with eight gradient estimation nodes. The horizontal gradients are isolated toward the northeast by the directional model.

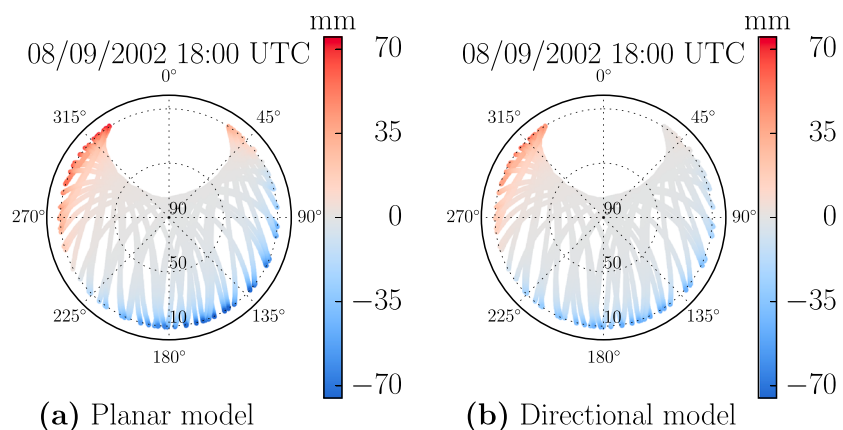


**Figure 13.** Horizontal gradient delays estimated at site CHRN using (a) the conventional planar model and (b) the directional model with eight gradient estimation nodes. The horizontal gradients are isolated toward the northwest by the directional model.

The gradient-induced delays recovered from a planar model (Figure 12a) provide some information about the spatial variability of the tropospheric delays: there is a strong gradient vector from the south of the MTPL site toward the north at the time of maximum precipitation (around 18:00 UTC). However, there is more information about this event that the planar gradient model has not been able to capture: the estimated delays derived by the directional model (Figure 12b) show a very clear isolated V shape, consistent with the V shape precipitation pattern seen in Figure 11, toward the northeast of the site, clearing out the positive gradients of the planar model toward the northwest. The V shape delay starts forming from the morning of the 8 September (even before the V shape precipitation forms), becomes stronger during the day, and reaches its maximum of about 75 mm (at 10° elevation angle) at around 18:00 UTC (which is about the same time when the precipitation also reaches its maximum). The isolated northeast gradient weakens throughout the rest of the day and the next day until it becomes similar to a planar eastward only gradient by the end of 9 September. Noticing the values of the delays at the maximum water vapor accumulation time (18:00 UTC) from the two models shows that the planar model underestimates the positive gradients toward the northeast (with a delay estimate of about 50 mm at 10° elevation) and overestimates the values of negative gradients toward the south of the site (with a delay estimate of about  $-60$  mm at 10° elevation), compared to the directional model with approximately 75 mm of positive delays toward the northeast and only  $-35$  mm toward the south at 10° elevation angle.

The estimated delays using the two models for the site CHRN, which lies in a different location with regard to the precipitation system, are shown in Figure 13 for the maximum precipitation time. The precipitation system is positioned mostly toward the northwest of the site CHRN during the event (Figures 11c–11f). Again, comparing the recovered gradients using the two models, it can be seen that the directional model has been able to isolate the gradients toward the northwest of the site, repairing the incorrect northeast gradients that are estimated by the planar model. While the differences in magnitudes of the gradients are small between the two models, the directional model reproduces a more accurate image of the tropospheric gradients (horizontal gradients toward the northwest, but no refractivity changes when moving toward the northeast of the station). This is consistent with the precipitation pattern observed in Figure 11d, in which there are high amounts of rainfall in the immediate northwest of CHRN, while the station falls in the southeastern border of the precipitation pattern with constant amounts of rainfall when moving to the northeast of the site. Also, while the planar model estimates large negative gradients toward the southeast (due to its linear assumption for the gradients), the directional model is more accurately displaying that the refractivity changes are small when moving toward the southeast of the station, which is also consistent with Figure 11d where there is no precipitation occurring in the southeastern side of CHRN at this epoch.

We have observed for the September 2002 heavy precipitation event that the use of our more sophisticated model of gradients helps to better understand the spatial variabilities of the tropospheric refractivity/water vapor for cases where there are complex patterns of moisture fields. However, the minimum elevation angle for the recorded observations at sites MTPL and CHRN for the case study of the southern France was 10°.

Also, it is unfortunate that the GPS satellite constellation hole falls in the northern side of the stations, where the most significant amounts of refractivity exist, and therefore, the impact of the directional gradient model is not sufficiently evident. The Gard region precipitation event shows the importance of using the directional model to estimate more realistic gradients but does not show much impact on positions and ZTDs, most likely because of the lack of low-elevation observations (particularly in azimuthal directions of large gradients) and/or possibly because of insufficiently strong gradients to show the effect on other parameters. In the next section, we examine another case study in California which contains observations at very low elevations, which is an appropriate case for examining the impact on positions and ZTD's.

## 5. Skewed Time Series of Plate Boundary Observatory Network

The Plate Boundary Observatory is a network of about 1100 GPS stations and other measuring devices such as seismometers and strainmeters mostly across the western United States which are operated by University NAVSTAR Consortium (UNAVCO) for EarthScope (<http://www.earthscope.org>) and supported by the National Science Foundation. While the main objective of the PBO network is deformation studies of the active boundary zone between the Pacific and North American Plates, the extended GPS network has introduced several geophysical applications including atmospheric studies [e.g., *Jackson, 2003; Larson et al., 2008*]. A well-known feature of some of the GPS stations of the PBO network, mostly concentrated around the Mammoth Lakes in the Sierra Nevada region in California, is the asymmetry of the time series that occurs throughout the year but is mostly observed during the winter time. The asymmetry appears as outliers in the position time series for several days with the most of outliers being in the same direction. *Materna and Herring [2013]* and *Materna [2014]* performed investigations on these skewed time series and speculated that the presence of Lee waves at some particular directions around the sites may be the cause.

Lee waves are internal gravity waves caused by the flow of stably stratified air over steep uneven topography, which leads to oscillations in the atmosphere for restoring the hydrostatic equilibrium. The relative humidity of a raised parcel of air by the oscillation increases, which may create clouds [e.g., *Glickman and Zenk, 2000*]. The very steep topography in the eastern side of Sierra Nevada Mountains (dropping from 4 km to 1 km in a horizontal range of around 10 km as noted by *Materna [2014]*) causes strong lee waves in this region, leading to large horizontal gradients of the humidity. Since the lee waves only appear in a small horizontal distance, the stations in the eastern side of the Sierra Nevada mountain ranges are expected to observe large horizontal tropospheric gradients on their western directions with not as large gradients in their eastern sides (Figure 14). This one-sided gradient scheme could be the cause for the asymmetric patterns seen in the position time series of the stations around the Mammoth Lakes in the Sierra Nevada region. The directional gradient model is, therefore, a potential tool to isolate these asymmetric horizontal gradients around the stations in this region.

Here we analyze the GPS time series of a set of PBO sites around the Mammoth Lakes (Figure 14) for the period 1 January 2012 to 30 March 2012, using both conventional planar and directional gradient models, in order to ascertain whether a more detailed gradient model is able to reduce the errors (and asymmetries) on position and ZTD estimates. The reference sites are chosen from the IGS core network such that we have stations in various directions around the PBO sites. Fortunately, most of the PBO RINEX files include very low elevation observations: we chose an elevation cutoff angle of  $3^\circ$  to reduce the correlations between the estimation parameters and also to assess the impact of gradients at low elevations. In addition, we derived and implemented the ESM in the same way as in section 4 (this time with 4 months of data) to remove any possible effect of site-specific errors such as multipath.

Having investigated the position time series of our selected GPS network resulted from using both the conventional planar and the new directional model, we found only marginal impacts of the directional model on horizontal components (consistent with our simulation results); therefore, we focus on the vertical component only for the rest of this case study. Figure 15a shows the scatter (WRMS) of the height time series for all the PBO stations in our analysis when using the directional model of gradients (black bars) compared to using the planar model (red bars). The stations in Figure 15 are sorted based on the WRMS of the planar solution. The height time series of the sites with higher scatters are generally improved in terms of WRMS, while the WRMS of the time series with low scatters are increased when using the directional model. For all the stations with WRMS of larger than 4 mm, except P654, the WRMS is reduced when taking advantage of the more complicated gradient model, with the largest improvements mainly for the worst sites. The increase in the WRMS



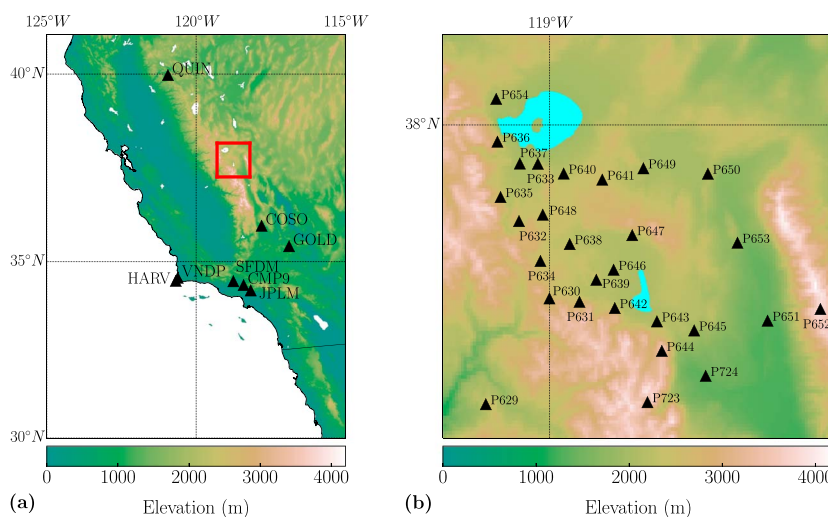


**Figure 14.** Sites from the plate boundary observatory network selected for the analyses and some of the far-field sites processed. (left) The red rectangle corresponds to the (right) frame location. The topography is retrieved from General Bathymetric Chart of the Oceans (GEBCO) 30'' grid.

of P654 is small and negligible compared to the reductions for other sites. For the majority of the stations with WRMS <4.0 mm, on the other hand, the directional model has led to more noisy height time series. This is an important finding, as it shows that for particular weather scenarios when the tropospheric refractivity field does not follow a plane around the station, the directional model is able to help in better modeling the gradients, while it results in higher dispersion at normal (i.e., planar) atmospheric conditions. This increased scatter of time series in normal situations is most likely because of larger number of correlated parameters estimated in the solution, which is overcome by the improvement in gradient modeling at abnormal conditions but not at typical close-to-planar situations.

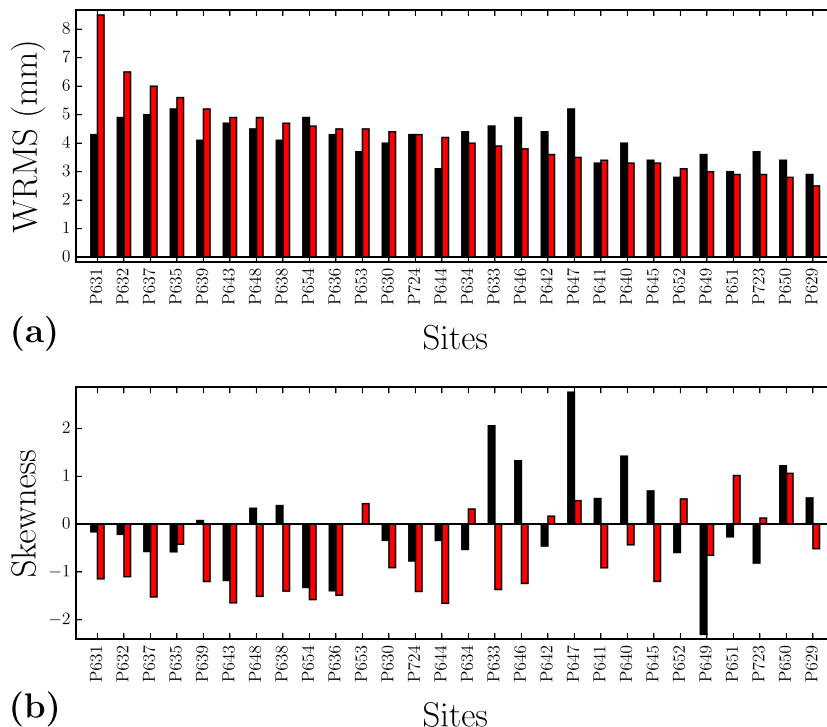


**Figure 15.** (a) WRMS and (b) skewness of the height position time series when using a directional gradient model (black bars) instead of a planar model (red bars), sorted based on WRMS of the planar gradient solution.



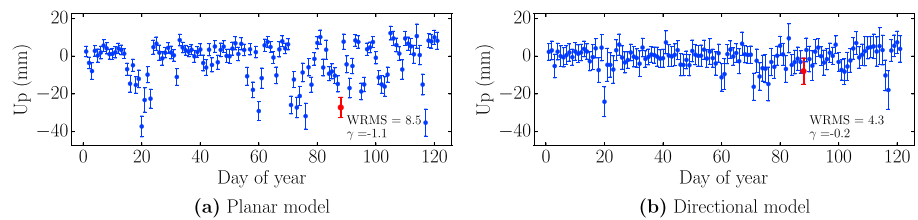


**Figure 16.** Time series of the vertical positions for site P631 and for the period of 1 January 2012 to 30 April 2012 when using (a) the conventional planar model of gradients compared to when using (b) the directional model for the gradients. WRMS and skewness ( $\gamma$ ) are shown on the figures, and the date 28 March 2012 is signified by red color.

*Materna* [2014] investigated more than 1000 PBO stations and noticed that the outliers in the position time series of each site are mainly in the same direction relative to the mean of the time series. For this reason, they used the concept of skewness as a statistical measure for studying the shape characteristics of the distribution of position estimates. Skewness is defined as the expected value of the third moment of a distribution; a skewed distribution has a longer tail either right or left of the distribution peak, which corresponds to the presence of positive or negative outliers in the relevant data series. Skewness is therefore an appropriate statistic for investigating the deviation of a distribution from a normal distribution and is useful for analyzing the skewed outliers in the position time series of the PBO sites. We use the same definition of the normalized sample skewness ( $\gamma$ ) as used by *Materna* [2014]:

$$\gamma = \frac{1}{N} \sum_{i=1}^N \left[ \left( \frac{X_i - \mu}{\sigma} \right)^3 \right] \quad (7)$$

where  $N$  is the number of data points,  $X_i$  is the  $i$ th data point, and  $\mu$  and  $\sigma$  are mean and standard deviation of the time series. The skewness values of the PBO GPS stations in our network are shown in Figure 15b in the same order that the WRMS values are displayed. There are a few interesting points to notice: The height time series which are highly scattered are usually also highly skewed; using the planar gradient model, about 79% of the stations with WRMS larger than 4 mm have skewness values (red bars in Figure 15b) of larger than 1. It is also worthwhile noting that about 71% of the sites in the analysis using the planar gradient model have negatively skewed height time series and, except for one station (P653), all the highly scattered height time series (with WRMS larger than 4 mm) are negatively skewed. Looking at the skewness values resulted from using the directional gradient model (black bars in Figure 15b), it is evident that the directional model has led to improvements in almost all of the highly scattered sites. The only exception to this is P635 which sees a degradation of only 0.4 in skewness; compare this to nine sites with reductions of larger than 1 and a reduction in the mean value of 1.10 for all the 13 highly scattered sites which are improved in terms of skewness. The degradation of the skewness for P635 despite the improvement in its WRMS is because the smaller standard deviation of the time series in the denominator of equation (7) has a larger effect on the skewness than the smaller deviations of individual points from the mean in the numerator, which results in a higher skewness. It is therefore important to note both WRMS and skewness statistics as the second and third moments of the distributions.

As an example of the improvements for individual time series, the height time series of site P631, which sees the largest reduction in the WRMS, are shown in Figure 16. The large improvement (from 8.5 mm to 4.3 mm WRMS) in the repeatability of the time series is clearly observed when using the directional model (Figure 16b) instead of the planar gradient model (Figure 16a). The skewness is also improved from  $-1.1$  for the planar model to only  $-0.2$  for the directional model. This reduction in skewness occurs because of several negative outliers having vanished by the use of directional gradient parametrization.

We assumed previously that the skewness in height time series results from abnormal atmospheric conditions (i.e., a tropospheric refractivity/water vapor field that is not well represented by a plane around the GPS station). We will now evaluate this assumption by taking as an example one day of the height time series of the site P631 (28 March 2012; colored in red in Figure 16) when there is a large error of about 20 mm introduced into the vertical component when using the conventional planar gradient model. The estimated delays due to gradients using the planar and the directional model for this single day are shown for 06:00 UTC in Figures 17a and 17b, respectively. The unusually large gradients (leading to larger than 120 mm of delay at  $10^\circ$  elevation)

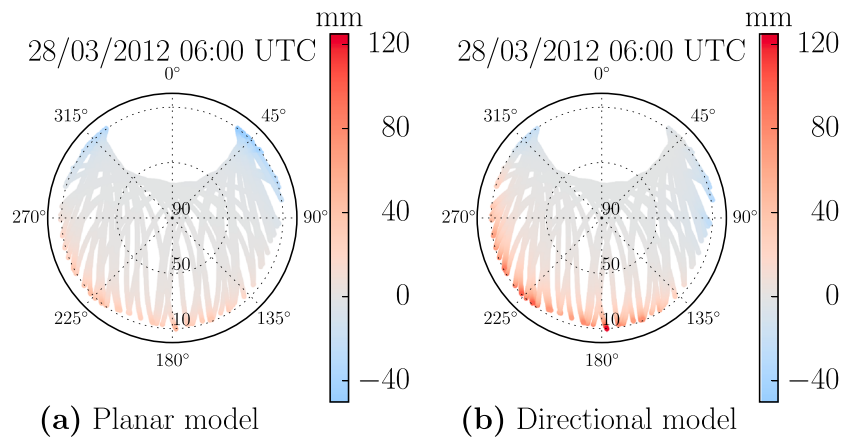


**Figure 17.** Horizontal gradient delays for site P631 at 06:00 UTC of 28 March 2012 estimated by (a) the planar and (b) the directional models for the gradients. Large horizontal gradients in the south of the station, captured by the directional model, are significantly underestimated by the planar model.

toward the southwest of the site captured by the directional gradient model are not fully recovered by the planar model, which explains the reason for the  $\sim 20$  mm error in the height estimate of the station when using the planar model. The planar model underestimates the positive gradients toward the southwest (with maximum delays estimated as  $\sim 50$  mm at  $10^\circ$  compared to  $\sim 120$  mm delay by the directional model) and overestimates the negative gradients toward the opposite direction (with the estimation of about  $-50$  mm of signal delay in the northeast compared to  $\sim -35$  mm delay by the directional model); this leads to the large bias in the estimation of vertical position observed in Figure 16. Using the directional model has resulted in much more accurate estimates of both southwestern positive gradients and northeastern negative gradients, leading to the large improvement in estimation of the vertical position for the same day. Therefore, there seems to be some tropospheric effect, not fully captured by the planar model but modeled by the directional approach, at the southwest of the site. This tropospheric moisture content could possibly be due to the presence of lee waves as suggested by *Materna* [2014].

The tropospheric zenith delay estimates are also affected by the mismodeling of the horizontal gradients. The estimates of tropospheric zenith wet delays using both planar and directional gradient models are shown in Figure 18 for the same day; there are differences of larger than 15 mm in the estimation of ZWD from the two solutions, which are well above the uncertainty level of the estimates. On average, the planar model overestimates the zenith wet delays by  $\sim 25\%$  in this day, which is a result of not considering very large gradients toward the southwest of the station (Figure 17). The significance of this finding is that in the generation of zenith total delays for meteorological applications, such as for assimilation into numerical weather prediction models, it is recommended to include low-elevation observations in order to decorrelate the height

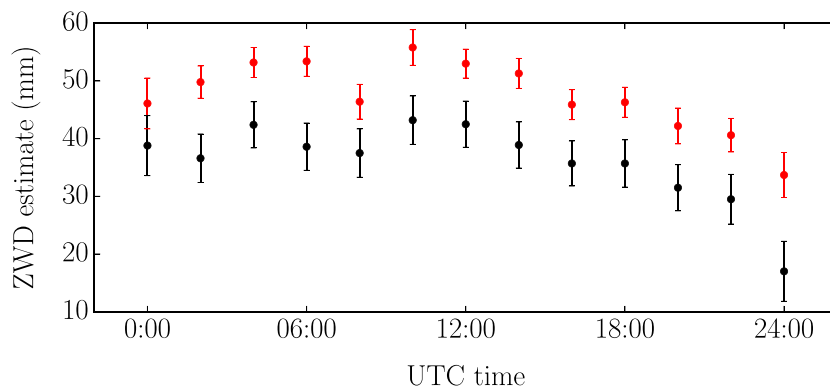


**Figure 18.** Two-hourly estimates of the zenith wet delays for site P631 on 28 March 2012 when using the planar model (red), compared to when using the directional model (black) for the gradients. On average, the planar model overestimates the zenith wet delays by  $\sim 25\%$  for this day.

and ZTD parameters: however, not having the proper gradient model in specific asymmetric gradient conditions results in further biases in ZTD when including the low-elevation observations. Therefore, using our proposed directional gradient model is recommended in these asymmetric situations to avoid such errors at low elevation angles.

The results from the PBO stations in the Sierra Nevada region provide us with more evidence on the importance of using a more complicated model of gradients than a planar assumption for refractivity field in abnormal asymmetric gradient conditions. Using the directional gradient model, reduction in both scatter and skewness of the height time series is evident, and the estimates of height and tropospheric zenith delay are improved in the days with abnormal gradient schemes. In normal (symmetric) gradient conditions, on the other hand, the directional model leads to higher dispersion of the estimated parameters as a result of larger number of correlated parameters. Horizontal positions are not much impacted by the new directional gradient model, which signifies that there might be some effects other than only tropospheric conditions for the skewness in time series of horizontal components.

## 6. Summary and Conclusions

In both simulations and real case studies analyzed in this paper we have shown that while the impact of mismodeled gradients is minimal on horizontal positions, it becomes highly significant for the estimation of heights and tropospheric zenith delays in particular weather scenarios. The conventional model of gradients introduced by *Chen and Herring* [1997] performs well in normal tropospheric situations, but its planar assumption for horizontal changes of tropospheric delay fails to accurately model the gradients in abnormal weather conditions when there are isolated gradients in some directions of a station. Such weather situations can happen as a result of topography-induced gravity waves in the atmosphere. As a result, estimation of both vertical positions and tropospheric zenith delays is contaminated by the mismodeled gradients. This may appear as outliers in the height time series of a GPS station and biases in the estimation of zenith total delays.

The proposed directional model developed and discussed in this paper is able to provide a more accurate representation of the tropospheric horizontal gradients during complicated atmospheric situations where tropospheric gradients are highly nonlinear. Application of the directional model results in significant improvements in the estimation of vertical position components (and correspondingly tropospheric zenith delays) for such highly heterogeneous weather conditions. For instance, the majority of outliers in skewed height time series of the Plate Boundary Observatory GPS stations in the Sierra Nevada region were removed by the directional gradient parametrization. Consequently, the directional gradient model is useful in the estimation of GPS vertical components and tropospheric delays in particular atmospheric conditions with highly nonlinear gradients.

The impact of using an improper model for the gradients on the estimated parameters is more pronounced when including low-elevation observations. It is therefore particularly important in meteorological applications, such as assimilation in numerical weather models, where low-elevation observations may be used for decorrelating the zenith delay parameters and the vertical position components, to take advantage of the more complicated model of directional gradients instead of the conventional planar model in atmospheric conditions when the refractivity field is highly heterogeneous. Since the impact of horizontal gradients are much larger on the slant GPS signals, in particular slant signals at low elevations, the use of the directional model for applications like GPS tomography that require the slant delay estimates will be useful.

The drawback of the directional model is the higher number of correlated parameters it introduces into the least squares inversion, causing higher dispersion of the estimated parameters in normal homogeneous tropospheric conditions. Therefore, it is important to note that the directional model should be used only when the tropospheric refractivity gradients are highly asymmetric. The modified GAMIT version developed in this study is capable of selecting different gradient models (planar model and directional model with different number of directional gradient parameters from 3 to 24) for each station and day but developing a technique to decide in advance how many number of gradient parameters to estimate for each station and day has yet to be developed.

Moreover, the analyses performed in this study were limited to the use of GPS observations, but the resolving power of the directional gradient model also depends on the amount of available data. Therefore, the impact

of incorporating other GNSS measurements (e.g., GLONASS, Galileo, and BeiDou) on the ability of a finer modeling of azimuthal heterogeneity of the water vapor field could be an interesting perspective for the future studies.

#### Acknowledgments

The authors would like to thank Thomas Herring for his advice and comments on the directional gradient model and its potential application in the Mammoth Lakes area and Michael Moore for providing the ESM code. We thank the three anonymous reviewers, whose constructive comments improved the manuscript. The first author would like to acknowledge Sebastien Allgeyer for his help with some of the Python scripts used for generation of the results in this paper. Figures in this paper were generated using Python and GMT software. The reanalysis data of rainfall for the case study of 8–9 September in southern France were obtained freely from the Système d'Extraction et de Visualisation des Données de l'Observatoire en Ligne (SEVNOL) (<http://sevnol.ohmcfv.fr>). The GPS daily RINEX observation files for the analyses of the two case studies in this paper were retrieved freely from UNAVCO (<ftp://data-out.unavco.org/pub/rinex/obs/>), RENAG (<ftp://renag.resif.fr/data/>), and EPNCB (<ftp://ftp.epncb.oma.be/pub/obs/>). The final orbit products were obtained freely from IGS (<ftp://cddis.gsfc.nasa.gov/gnss/products/>). The topographic data for the California region were downloaded freely from GEBCO ([http://www.gebco.net/data\\_and\\_products/gridded\\_bathymetry\\_data/](http://www.gebco.net/data_and_products/gridded_bathymetry_data/)).

#### References

- Altamimi, Z., X. Collilieux, and L. Métivier (2011), ITRF2008: An improved solution of the international terrestrial reference frame, *J. Geod.*, *85*(8), 457–473.
- Bennett, G. V., and A. Jupp (2012), Operational assimilation of GPS zenith total delay observations into the Met Office numerical weather prediction models, *Mon. Weather Rev.*, *140*(8), 2706–2719.
- Bevis, M., S. Businger, T. A. Herring, C. Rocken, R. A. Anthes, and R. H. Ware (1992), GPS meteorology: Remote sensing of atmospheric water vapor using the Global Positioning System, *J. Geophys. Res.*, *97*(D14), 157,87–15,801.
- Böhm, J., M. Ess, and H. Schuh (2005), Asymmetric mapping functions for CONT02 from ECMWF, in *Proceedings of the 17th Working Meeting on European VLBI for Geodesy and Astrometry*, edited by M. Vennebusch and A. Nothnagel, pp. 64–68, Istituto di Radioastronomia, Noto, Italy.
- Böhm, J., A. Niell, P. Tregoning, and H. Schuh (2006a), Global Mapping Function (GMF): A new empirical mapping function based on numerical weather model data, *Geophys. Res. Lett.*, *33*, L07304, doi:10.1029/2005GL025546.
- Böhm, J., B. Werl, and H. Schuh (2006b), Troposphere mapping functions for GPS and very long baseline interferometry from European Centre for Medium-Range Weather Forecasts operational analysis data, *J. Geophys. Res.*, *111*, B02406, doi:10.1029/2005JB003629.
- Boudevillain, B., G. Delrieu, B. Galabertier, L. Bonnifait, L. Bouilloud, P.-E. Kirstetter, and M.-L. Mosini (2011), The Cévennes-Vivarais Mediterranean Hydrometeorological Observatory database, *Water Resour. Res.*, *47*, W07701, doi:10.1029/2010WR010353.
- Brenot, H., V. Ducrocq, A. Walpersdorf, C. Champollion, and O. Caumont (2006), GPS zenith delay sensitivity evaluated from high-resolution numerical weather prediction simulation of the 8–9 September 2002 flash flood over southeastern France, *J. Geophys. Res.*, *111*, D15105, doi:10.1029/2004JD005726.
- Champollion, C., F. Masson, J. Van Baelen, A. Walpersdorf, J. Chéry, and E. Doerflinger (2004), GPS monitoring of the tropospheric water vapor distribution and variation during the 9 September 2002 torrential precipitation episode in the Cévennes (southern France), *J. Geophys. Res.*, *109*, D24102, doi:10.1029/2004JD004897.
- Chen, G., and T. A. Herring (1997), Effects of atmospheric azimuthal asymmetry on the analysis of space geodetic data, *J. Geophys. Res.*, *102*(B9), 20,489–20,502.
- Davis, J. L., T. A. Herring, I. I. Shapiro, A. E. Rogers, and G. Elgered (1985), Geodesy by radio interferometry: Effects of atmospheric modeling errors on estimates of baseline length, *Radio Sci.*, *20*(6), 1593–1607.
- Davis, J. L., G. Elgered, A. E. Niell, and C. E. Kuehn (1993), Ground-based measurement of gradients in the “wet” radio refractivity of air, *Radio Sci.*, *28*(6), 1003–1018.
- Delrieu, G., et al. (2005), The catastrophic flash-flood event of 8–9 September 2002 in the Gard region, France: A first case study for the Cévennes-Vivarais Mediterranean Hydrometeorological Observatory, *J. Hydrometeorol.*, *6*(1), 34–52.
- Delrieu, G., A. Wijbrans, B. Boudevillain, D. Faure, L. Bonnifait, and P.-E. Kirstetter (2014), Geostatistical radar–raingauge merging: A novel method for the quantification of rain estimation accuracy, *Adv. Water Resour.*, *71*, 110–124.
- Dow, J. M., R. E. Neilan, and C. Rizos (2009), The international GNSS service in a changing landscape of Global Navigation Satellite Systems, *J. Geod.*, *83*(3–4), 191–198.
- Eriksson, D., D. S. MacMillan, and J. M. Gipson (2014), Tropospheric delay ray tracing applied in VLBI analysis, *J. Geophys. Res. Solid Earth*, *119*, 9156–9170, doi:10.1002/2014JB011552.
- Gardner, C. (1976), Effects of horizontal refractivity gradients on the accuracy of laser ranging to satellites, *Radio Sci.*, *11*(12), 1037–1044.
- Gegout, P., R. Biancale, and L. Soudarin (2011), Adaptive mapping functions to the azimuthal anisotropy of the neutral atmosphere, *J. Geod.*, *85*(10), 661–677.
- Glickman, T. S., and W. Zenk (2000), *Glossary of Meteorology*, Am. Meteorol. Soc., Boston, Mass.
- Herring, T. (1992), Modeling atmospheric delays in the analysis of space geodetic data, in *Proceedings of Refraction of Transatmospheric Signals in Geodesy*, vol. 36, edited by J. C. De Munck and T. A. Spoelstra, pp. 157–164, Netherlands Geodetic Commission Publ. on Geod., The Hague, Netherlands.
- Herring, T., R. King, M. Floyd, and S. McClusky (2015), GAMIT reference manual: GPS Analysis at MIT, release 10.6, Department of Earth, Atmospheric, and Planetary Sciences, Massachusetts Institute of Technology, Cambridge, Mass.
- Hobiger, T., R. Ichikawa, T. Takasu, Y. Koyama, and T. Kondo (2008), Ray-traced troposphere slant delays for precise point positioning, *Earth Planets Space*, *60*(5), e1–e4.
- Jackson, M. E. (2003), Geophysics at the speed of light: EarthScope and the Plate Boundary Observatory, *Leading Edge*, *22*(3), 262–267.
- Labbouz, L., J. Van Baelen, and C. Duroure (2015), Investigation of the links between water vapor field evolution and rain rate based on 5 years of measurements at a midlatitude site, *Geophys. Res. Lett.*, *42*, 9538–9545, doi:10.1002/2015GL066048.
- Landskron, D., A. Hofmeister, and J. Böhm (2015), *Refined Tropospheric Delay Models for CONT11*, pp. 1–5, Springer, Berlin.
- Larson, K. M., E. E. Small, E. D. Gutmann, A. L. Bilich, J. J. Braun, and V. U. Zavorotny (2008), Use of GPS receivers as a soil moisture network for water cycle studies, *Geophys. Res. Lett.*, *35*, L24405, doi:10.1029/2008GL036013.
- Lyard, F., F. Lefevre, T. Letellier, and O. Francis (2006), Modelling the global ocean tides: Modern insights from FES2004, *Ocean Dyn.*, *56*(5–6), 394–415.
- MacMillan, D. S. (1995), Atmospheric gradients from very long baseline interferometry observations, *Geophys. Res. Lett.*, *22*(9), 1041–1044.
- Marini, J. W. (1972), Correction of satellite tracking data for an arbitrary tropospheric profile, *Radio Sci.*, *7*(2), 223–231.
- Materna, K. (2014), Analysis of atmospheric delays and asymmetric positioning errors in the global positioning system, Bachelor's thesis, Massachusetts Inst. of Technol., Cambridge, Mass.
- Materna, K., and T. Herring (2013), Analysis of skewed GPS position estimates: Effects of coupling local topography and atmospheric conditions. Abstracts G53A-0907 presented at 2013 Fall Meeting, AGU, San Francisco, Calif., 9–13 Dec.
- Moore, M., C. Watson, M. King, S. McClusky, and P. Tregoning (2014), Empirical modelling of site-specific errors in continuous GPS data, *J. Geod.*, *88*(9), 887–900.
- Niell, A. E. (1996), Global mapping functions for the atmosphere delay at radio wavelengths, *J. Geophys. Res.*, *101*(B2), 3227–3246.
- Rothacher, M., and G. Beutler (1998), The role of GPS in the study of global change, *Phys. Chem. Earth*, *23*(9), 1029–1040.
- Saastamoinen, J. (1972), Atmospheric correction for the troposphere and stratosphere in radio ranging satellites, in *The Use of Artificial Satellites for Geodesy*, edited by S. W. Henriksen, A. Mancini, and B. H. Chovitz, pp. 247–251, AGU, Washington, D. C.

- Schmid, R., R. Dach, X. Collilieux, A. Jäggi, M. Schmitz, and F. Dilssner (2016), Absolute IGS antenna phase center model igs08.atx: Status and potential improvements, *J. Geod.*, *90*(4), 343–364.
- Tregoning, P., and C. Watson (2009), Atmospheric effects and spurious signals in GPS analyses, *J. Geophys. Res.*, *114*, B09403, doi:10.1029/2009JB006344.
- Tregoning, P., R. Boers, D. O'Brien, and M. Hendy (1998), Accuracy of absolute precipitable water vapor estimates from GPS observations, *J. Geophys. Res.*, *103*(D22), 28,701–28,710.
- Van Baelen, J., M. Reverdy, F. Tridon, L. Labbouz, G. Dick, M. Bender, and M. Hagen (2011), On the relationship between water vapour field evolution and the life cycle of precipitation systems, *Q. J. R. Meteorol. Soc.*, *137*(S1), 204–223.